

This manuscript has been submitted for publication in *Geophysical Research Letters*. Please note, it has not yet been accepted for publication. Subsequent versions of this manuscript may have slightly different content. If accepted, the final version of this manuscript will be available via the 'Peer-reviewed Publication DOI' link on the right-hand side of this webpage. Please feel free to contact the authors; we welcome any feedback.

1 **Wind-driven evolution of the North Pacific subpolar gyre over the last**  
2 **deglaciation**

3

4 William R Gray<sup>1,2\*</sup>, Robert CJ Wills<sup>3</sup>, James WB Rae<sup>2</sup>, Andrea Burke<sup>2</sup>, Ruza F  
5 Ivanovic<sup>4</sup>, William HG Roberts<sup>5</sup>, David Ferreira<sup>6</sup>, Paul J Valdes<sup>7</sup>

6 <sup>1</sup>Laboratoire des Sciences du Climat et de l'Environnement (LSCE/IPSL), Gif-sur-  
7 Yvette, France

8 <sup>2</sup>School of Earth and Environmental Science, University of St Andrews, UK

9 <sup>3</sup>Department of Atmospheric Sciences, University of Washington, USA

10 <sup>4</sup>School of Earth & Environment, University of Leeds, UK

11 <sup>5</sup>Geography and Environmental Sciences, Northumbria University, UK

12 <sup>6</sup>Department of Meteorology, University of Reading, UK

13 <sup>7</sup>School of Geographical Sciences, University of Bristol, UK

14

15 \*corresponding author: [william.gray@lsce.ipsl.fr](mailto:william.gray@lsce.ipsl.fr)

16

17 *Key points*

- 18 • Planktic foraminiferal  $\delta^{18}\text{O}$  data indicate that the North Pacific subpolar gyre  
19 expanded southward by  $\sim 3^\circ$  during the Last Glacial Maximum
- 20 • Climate models show that changes in gyre extent/strength are driven by the  
21 response of the westerlies to ice sheet albedo and topography
- 22 • Proxy data and model simulations indicate that the gyre boundary and winds  
23 began to migrate northward at  $\sim 17$ -16 ka, during Heinrich Stadial 1

24

25 *Abstract*

26 North Pacific atmospheric and oceanic circulations are key missing pieces in  
27 our understanding of the reorganisation of the global climate system since the Last  
28 Glacial Maximum (LGM). Here, using a basin-wide compilation of planktic  
29 foraminiferal  $\delta^{18}\text{O}$ , we show that the North Pacific subpolar gyre extended  $\sim 3^\circ$  further  
30 south during the LGM, consistent with sea surface temperature and productivity proxy  
31 data. Analysis of an ensemble of climate models indicates that the expansion of the  
32 subpolar gyre was associated with a substantial gyre strengthening. These gyre  
33 circulation changes were driven by a southward shift in the mid-latitude westerlies and  
34 increased wind-stress from the polar easterlies. Using single-forcing model runs, we  
35 show these atmospheric circulation changes are a non-linear response to the combined  
36 topographic and albedo effects of the Laurentide Ice Sheet. Our reconstruction suggests  
37 the gyre boundary (and thus westerly winds) began to migrate northward at  $\sim 17$ -16 ka,  
38 during Heinrich Stadial 1.

39

#### 40 *Plain language summary*

41 Despite the North Pacific's importance in the global climate system, changes in  
42 the circulation of this region since the last ice age are poorly understood. Today, the  
43 North Pacific Ocean has very different properties north and south of  $\sim 40^\circ\text{N}$ : to the  
44 south, the warm surface waters form a circulation cell that moves clockwise (the  
45 subtropical gyre); to the north, the cold surface waters form a circulation cell that moves  
46 anti-clockwise (the subpolar gyre). This difference in surface ocean circulation north  
47 and south of  $\sim 40^\circ\text{N}$  is determined by the wind patterns. Here, using a compilation of  
48 oxygen isotopes measured in the carbonate shells of fossil plankton from sediment  
49 cores across the basin, which tracks changes in the spatial pattern of temperature, we  
50 reconstruct how the position of the boundary between the gyres changed since the last

51 ice age. Our results show that the boundary between the gyres was shifted southward  
52 by  $\sim 3^\circ$  during the last ice age; this indicates that the westerly winds were also shifted  
53 southward at this time. Using numerical simulations of the climate, we find that this ice  
54 age shift in the westerly winds is primarily due to the presence of a large ice sheet over  
55 North America.

56

## 57 **1. Introduction**

58 Despite the North Pacific's importance in the global climate system, the  
59 reorganisation of surface ocean and atmosphere in this region during the Last Glacial  
60 Maximum (LGM,  $\sim 20$  ka) and the last deglaciation ( $\sim 10$ - $20$  ka, 'the deglaciation' from  
61 here on) remain poorly constrained. Changes in atmospheric and surface ocean  
62 circulation within the North Pacific are potentially important drivers of observed  
63 changes in the overturning circulation and biogeochemistry of the North Pacific during  
64 the LGM and deglaciation, suggested to play a role in regulating atmospheric CO<sub>2</sub>  
65 (Keigwin, 1998; Okazaki *et al.*, 2010; Rae *et al.*, 2014; Gray *et al.*, 2018). The  
66 overturning and gyre circulations are also important influences on poleward ocean heat  
67 transport. Large changes in the hydroclimate of western North America during the  
68 LGM and the deglaciation (e.g. Oviatt *et al.*, 1999; Nelson *et al.*, 2005; Lyle *et al.*,  
69 2012; McGee *et al.*, 2012; Kirby *et al.*, 2013; Ibarra *et al.*, 2014) have been suggested  
70 to result from the reorganisation of North Pacific atmospheric circulation (e.g. Oster *et*  
71 *al.*, 2015; Wong *et al.*, 2016; Lora *et al.*, 2017; Lora, 2018), with early modelling work  
72 suggesting a southward displacement of the westerly jet with the presence of the  
73 Laurentide Ice Sheet (Manabe & Broccoli, 1985; Bartlein *et al.*, 1998). However,  
74 evidence for this atmospheric reorganisation has not yet been identified in marine  
75 records.



76

77           Driven by the opposite signs of the climatological wind stress curl ( $\nabla \times \tau$ ), the  
78 subtropical and subpolar gyres of the North Pacific Ocean have vastly different physical  
79 and chemical properties (Boyer *et al.*, 2013; Key *et al.*, 2015). The boundary between  
80 the gyres (defined as the point between the gyres at which the barotropic streamfunction  
81 [ $\Psi_{\text{barotropic}} = 0$ ] is determined by Sverdrup balance and occurs where  $\nabla \times \tau$  integrated  
82 from the eastern boundary of the basin is zero (Sverdrup, 1947; Deser *et al.*, 1999).  
83 Today, the gyre boundary (which broadly determines the position of the subarctic front)  
84 is nearly zonal and lies at  $\sim 40^\circ\text{N}$ , approximately following the local  $\nabla \times \tau = 0$  line.  
85 South of  $\sim 40^\circ\text{N}$ , anticyclonic wind stress curl in the subtropical gyre (STG) results in  
86 Ekman pumping (downwelling), allowing warm, nutrient-poor, surface waters to  
87 accumulate. North of  $\sim 40^\circ\text{N}$ , cyclonic wind stress curl in the subpolar gyre (SPG)  
88 results in Ekman suction (upwelling), bringing cold, nutrient-rich, waters from the  
89 oceans interior into the surface. Surface ocean chlorophyll concentrations are order of  
90 magnitude higher in the SPG compared to the STG. The gyre circulation also dominates  
91 ocean heat transport in the Pacific (Forget and Ferreira, 2019). The relative extent and  
92 the strength of the gyres therefore exerts a large influence over basin-wide ecology,  
93 biogeochemistry, and climate.

94

95           Coupled climate models predict a  $\sim 60\%$  increase in wind stress curl within the  
96 subpolar North Pacific under glacial forcings compared to pre-industrial forcings (Gray  
97 *et al.*, 2018). By Sverdrup balance (Sverdrup, 1947), this should result in a large and  
98 predictable response in gyre circulation. Despite some early work suggesting the  
99 subarctic front may have shifted southward during glacial times (Thompson and  
100 Shackleton, 1980; Sawada and Handa, 1998), little is known about gyre circulation over

101 the deglaciation. Here, we use meridional profiles of planktic foraminiferal  $\delta^{18}\text{O}$  to  
102 reconstruct the position of the gyre boundary over the deglaciation. Given the relatively  
103 simple dynamical link between gyre circulation and wind stress, our gyre boundary  
104 reconstruction also helps constrain the deglacial reorganisation of the atmospheric  
105 circulation. We use an ensemble of climate models forced by a range of boundary  
106 conditions to further explore the causes and implications of our gyre boundary  
107 reconstruction for the atmospheric and near-surface ocean circulations within the North  
108 Pacific.

109

## 110 **2. Methods**

### 111 *2.1 $\delta^{18}\text{O}$ as a tracer of gyre circulation*

112 The large ( $\sim 20$  °C) sea surface temperature (SST) difference between the gyres  
113 (Boyer *et al.*, 2013) allows us to use meridional profiles of  $\delta^{18}\text{O}$  in planktic  
114 foraminiferal calcite ( $\delta^{18}\text{O}_{\text{calcite}}$ ) to trace the gyre boundary (supporting information).  
115 This temperature difference between the gyres drives a calcite-water fractionation  
116 ( $\delta^{18}\text{O}_{\text{calcite-water}}$ ) that is  $\sim 6$  ‰ greater in the SPG than the STG (Figure 1d). Therefore,  
117 although the  $\delta^{18}\text{O}$  of seawater ( $\delta^{18}\text{O}_{\text{water}}$ ) is  $\sim 1$  ‰ lighter in the SPG compared to the  
118 STG due to its lower salinity ( $\sim 1.5$  PSU; Figure 1c),  $\delta^{18}\text{O}_{\text{calcite}}$  is  $\sim 5$  ‰ higher in the  
119 SPG than the STG (Figure 1e). The two gyres are thus clearly delineated in the  $\delta^{18}\text{O}$  of  
120 planktic foraminiferal calcite predicted using modern temperature and  $\delta^{18}\text{O}_{\text{water}}$  (Figure  
121 1e), with the steepest meridional gradient in  $\delta^{18}\text{O}_{\text{calcite}}$  at the gyre boundary (Figure 1f).  
122 While there are likely to be local changes in  $\delta^{18}\text{O}_{\text{water}}$  across the basin over the  
123 deglaciation, a salinity difference of  $\sim 15$  PSU would be required to equal the  
124 temperature signal between the gyres. As no mechanism exists to drive such a  
125 salinity/ $\delta^{18}\text{O}_{\text{water}}$  difference, temperature will always dominate the meridional  $\delta^{18}\text{O}_{\text{calcite}}$

126 gradient (Figure 1f). We can therefore use meridional profiles of  $\delta^{18}\text{O}_{\text{calcite}}$  to track the  
127 position of the gyre boundary.

128

129 We compiled previously published planktic foraminiferal  $\delta^{18}\text{O}_{\text{calcite}}$  records  
130 spanning the last deglaciation from the North Pacific Ocean (Figure 1; supporting  
131 information). The gyre boundary is clearly defined by the steepest meridional gradient  
132 ( $\Delta\delta^{18}\text{O}_{\text{calcite}}/\Delta\text{Latitude}$ ) in the Holocene planktic foraminiferal  $\delta^{18}\text{O}_{\text{calcite}}$  data (Figure 2;  
133 supporting information). The difference in meridional temperature gradient between  
134 the east and west of the basin is also evident in the Holocene  $\delta^{18}\text{O}_{\text{calcite}}$  data (Figure 2b).

135

136 To reconstruct position the of gyre boundary over the deglaciation, we first  
137 model the  $\delta^{18}\text{O}_{\text{calcite}}$  data as a function of latitude, using a general additive model  
138 (GAM) in the *mgcv* package in R (Wood, 2011; Wood *et al.*, 2016) at 500 yr timesteps  
139 from 18.5 to 10.5 ka (supporting information; Figures S2-4). The smoothing term was  
140 calculated using generalised cross validation (GCV), and corroborated using Reduced  
141 Maximum Likelihood (REML), with both methods resulting in near-identical  
142 smoothing terms and model fits. We then calculate the change in gyre boundary  
143 position over the deglaciation as the latitudinal shift ( $x^\circ$ ) that minimises the Euclidian  
144 distance ( $L^2$ ) between the Holocene (taken as  $10.5\pm 0.5$  ka)  $\delta^{18}\text{O}_{\text{calcite}}(\text{Lat})$  GAM fit and  
145 the GAM fit at each time step, computed within a  $5^\circ$  latitudinal band around the  
146 maximum meridional  $\delta^{18}\text{O}_{\text{calcite}}$  gradient in the Holocene data (supporting information;  
147 Figure S5). The width of this latitudinal band has a negligible effect on our results  
148 (Figure S6).

149

150 We account for the effect of whole ocean changes in sea level ( $\delta^{18}\text{O}_{\text{water}}$ ) and  
151 SST on  $\delta^{18}\text{O}_{\text{calcite}}$  by subtracting the 1‰ whole ocean change in  $\delta^{18}\text{O}_{\text{water}}$  (Schrag *et al.*,  
152 2002) and the  $\sim 2^\circ\text{C}$  global-mean change in SST from the PMIP3 climate model  
153 ensemble (see below), scaling the subtracted anomalies through time in proportion to  
154 the sea level curve of Lambeck *et al.* (2014). This scaling is most robust for  $\delta^{18}\text{O}_{\text{water}}$   
155 due to its direct correlation with global terrestrial ice volume, however the correction  
156 for global SST has very little effect and is not therefore a significant source of error.  
157 We opt to make this global-mean SST correction in order to minimise differences in  
158  $\delta^{18}\text{O}_{\text{calcite}}$  at different time steps relating to whole-ocean SST changes (i.e. from  
159 radiative forcing), rather than local SST anomalies. The calculated changes in gyre  
160 boundary position ( $\Delta\text{Lat}$ ) are given in table S2; the reported uncertainty in  $\Delta\text{Lat}$  is  
161 derived by quadratically propagating the uncertainty in the  $\delta^{18}\text{O}_{\text{calcite}}(\text{Lat})$  GAM fits,  
162 and is typically  $\pm 0.9^\circ$  ( $1\sigma$ ).

163

## 164 2.2 General circulation models

165 We analysed an ensemble of general circulation models forced with pre-  
166 industrial and glacial boundary conditions from the Coupled Model Intercomparison  
167 Project phase 5 (CMIP5, Taylor *et al.* 2012) and the Paleoclimate Model  
168 Intercomparison Project phase 3 (PMIP3, Braconnot *et al.* 2012). We include all four  
169 models for which both wind stress and barotropic stream function are available  
170 (supporting information). We also analyse results from a single model (HadCM3)  
171 where LGM greenhouse gases, ice sheet topography (‘green mountains’), and ice sheet  
172 albedo (‘white plains’) forcing were changed individually (Roberts and Valdes, 2017),  
173 as well as a series of HadCM3 runs where all forcings and boundary conditions are  
174 changed progressively over the deglaciation in 500 yr ‘snapshots’ (as used by Morris

175 *et al.*, 2018), broadly following the PMIP4 protocol (Figure S8; see Ivanovic *et al.*,  
176 2016 and supporting information).

177

### 178 **3. Results and Discussion**

#### 179 *3.1 LGM planktic foraminiferal $\delta^{18}O$ , SST, and productivity*

180 While sites that today are located well within either the modern SPG or STG  
181 display an LGM difference in  $\delta^{18}O_{\text{calcite}}$  of  $\sim 1\text{-}1.5\text{‰}$ , sites located within the transition  
182 zone between the gyres display a much greater change of up to  $\sim 3\text{‰}$  (Figure 1). This  
183 anomalously large glacial increase in  $\delta^{18}O_{\text{calcite}}$  is observed in transition zone sites in  
184 the east and west of the basin. The Holocene  $\delta^{18}O_{\text{calcite}}$  of sites located in today's  
185 transition zone typically falls about half-way between the  $\delta^{18}O_{\text{calcite}}$  of the SPG and  
186 STG. In contrast, during the LGM the  $\delta^{18}O_{\text{calcite}}$  of these same sites is almost identical  
187 to the  $\delta^{18}O_{\text{calcite}}$  of sites located well within the SPG. This pattern is indicative of a  
188 southward shift in the boundary between the SPG and STG, such that sites that are  
189 located within the transition zone today were located in (or felt a much greater influence  
190 of) the SPG during the LGM.

191

192 Analysing all data from across the basin together indicates the gyre boundary  
193 was positioned  $3.1 \pm 0.9^\circ$  ( $1\sigma$ ) further south during the LGM compared with its position  
194 in the Holocene (Figure 2a). Analysing the data from east and west of  $180^\circ$  separately  
195 results in a smaller change in the west of  $2.0 \pm 0.9^\circ$ , and a greater change in the east of  
196  $6.0 \pm 1.1^\circ$  (Figure 2b). To assess if the larger change in the east of the basin may be an  
197 artefact of changes in coastal upwelling, a process which could also influence the local  
198 SST (and thus  $\delta^{18}O_{\text{calcite}}$ ) anomaly, we compare the PMIP3 ensemble mean SST near  
199 the eastern boundary of the basin to the zonal mean, and zonal mean east of  $180^\circ$  (Figure

200 S9). This analysis demonstrates no anomalous cooling at the eastern margin of the basin  
201 relative to the zonal average and zonal average east of 180° in the models, suggesting  
202 that coastal upwelling is unlikely to have a significant effect on our reconstruction. It  
203 is more difficult to track the position of the gyre boundary in the east because of the  
204 gentler slope of the meridional temperature gradient and fewer number of sites.  
205 However, Sverdrup balance implies that the gyre boundary in the west of the basin  
206 should respond to the integrated wind stress curl across the entire basin. Therefore, the  
207 observation of a southward shift in the basin-wide gyre boundary observed in the west  
208 holds regardless of how we interpret changes in the east of the basin.

209

210         Compiling all available Mg/Ca and  $U^{k_{37}}$  SST data (supporting information)  
211 reveals a very similar pattern of temperature changes to the foraminiferal  $\delta^{18}O$  data  
212 (Figure 2c). At the LGM, the SPG shows a slight warming or no change and the STG  
213 shows a slight cooling, while transition zone sites on both the east and west of the basin  
214 show an anomalously large cooling, supporting the southward extension of cold  
215 subpolar waters during glacial times.

216

217         Analysing the North Pacific %Opal compilation of Kohfeld and Chase (2011)  
218 over the last deglaciation reveals that, while the SPG and STG show a decrease in  
219 %Opal during the LGM, sites in the transition zone show a ~25% increase in %Opal  
220 on both sides of the basin (Figure 2d). This pattern is consistent with nutrient-rich  
221 subpolar waters moving further south during the LGM and increasing local  
222 productivity. The southward extension of the SPG provides a solution to the long-  
223 standing question of why, while productivity decreased throughout the SPG during  
224 LGM, it increased in the modern day location of the transition zone between the gyres

225 (Kienast *et al.*, 2004), leading to an anti-phased pattern of productivity between the  
226 SPG and transition zone over glacial-interglacial cycles (Figure S10).

227

### 228 3.2 LGM General Circulation Model Simulations

229 Every model within the PMIP3 ensemble analysed exhibits a southward shift of  
230 the gyre boundary under glacial forcings relative to pre-industrial, with an ensemble  
231 mean change of  $2.7^\circ$  in the zonal-mean position of  $\Psi_{\text{barotropic}} = 0$  (Figures 3 and 4), in  
232 excellent agreement with our reconstruction. Consistent with the proxy data, most  
233 models show a greater shift in the east of the basin, with a model mean southward shift  
234 of  $3.4^\circ$ , and a smaller change in the west of  $2.3^\circ$  (Fig. 4c). In the models this southward  
235 shift in the southern boundary of the SPG is caused by an overall expansion of the gyre;  
236 there is no change in the location of the northern edge of the gyre, which remains at the  
237 northern boundary of the basin. In addition to the expansion of the gyre, the models  
238 show a substantial increase in gyre strength, with an ensemble mean  $\Psi_{\text{barotropic}}$  increase  
239 of 8.2 Sv (maximum north of  $40^\circ$ ). The expansion and strengthening of the subpolar  
240 gyre circulation appear tightly coupled across all models and forcings (Figure 4). This  
241 coupling of the expansion and strengthening of the gyre arises as both processes are  
242 driven by changes in wind stress curl, rather than through a mechanistic link based on  
243 gyre dynamics.

244

245 The PMIP3 ensemble demonstrates a  $2.8^\circ$  southward shift in the latitude of  
246 maximum westerly wind stress in the east of the basin, but little change in the west of  
247 the basin (Figure 3); this southward shift the westerly winds is in keeping with early  
248 modelling work which demonstrated a southward displacement of the westerly jet  
249 during the LGM (e.g. Manabe & Broccoli, 1985; Bartlein *et al.*, 1998). A southward

250 shift in the position of the easterlies – such that they blow over the northern boundary  
251 of the North Pacific during the LGM, rather than over the Bering Straits and Sea as they  
252 do today (Gray *et al.*, 2018) – drives a large increase in the zonal wind stress over the  
253 subpolar gyre (50% increase in the west of the basin and 100% increase in the east of  
254 the basin). The combined effect of the increase in easterly wind stress and the  
255 southward shift and increase in westerly wind stress is a large increase in wind stress  
256 curl across the subpolar gyre (Gray *et al.*, 2018), with a southward expansion in positive  
257 wind stress curl in the east of the basin. This southward expansion in positive wind  
258 stress curl in the east drives the southward expansion of the subpolar gyre across the  
259 entire basin because the circulation is, to a good approximation, in Sverdrup balance  
260 and therefore reflects the zonal integral of  $\nabla \times \tau$  from the eastern boundary of the basin  
261 (Sverdrup, 1947; Hautala *et al.*, 1994; Deser *et al.*, 1999; Wunsch, 2011).

262

263 To investigate which forcing(s) ultimately drive the wind stress and gyre  
264 circulation changes during the LGM, we analysed HadCM3 model runs with individual  
265 LGM forcings from greenhouse gases, ice sheet albedo, ice sheet topography, and  
266 combined ice sheet albedo and topography (Figure 4). Substantial changes in the  
267 position of  $\nabla \times \tau = 0$  and  $\Psi_{\text{barotropic}} = 0$  are only seen with the combined effects of ice  
268 sheet topography and albedo; ice sheet topography or ice sheet albedo alone have very  
269 little effect, as do greenhouse gases. This result illustrates a large non-linearity in the  
270 response of atmospheric circulations to ice sheet forcing; this is the result of the distinct  
271 and differing seasonality in the response of the atmosphere over the Pacific to ice sheet  
272 forcing, with albedo having the greatest effect in summer and topography having the  
273 greatest effect in winter (Roberts *et al.*, 2019). Note that a further shift in the gyre  
274 boundary is seen with the addition of greenhouse gas forcing (Figure 4), again



275 exceeding that expected from the sum of the individual responses and suggesting a  
276 further non-linear response to the combined ice sheet and greenhouse gas forcings (e.g.  
277 Broccoli and Manabe, 1987).

278

279 The expansion of the subpolar gyre, and associated cold waters, drives a large  
280 cooling in the mid-latitudes south of the modern-day gyre boundary. The contraction  
281 and expansion of the gyre therefore act to amplify temperature changes in the mid-  
282 latitudes over glacial-interglacial cycles. The strengthening of the SPG would increase  
283 poleward heat transport and may play a role in driving the relative warmth of the SPG  
284 during the LGM (Figure 2). A modern analogue is the Pacific Decadal Oscillation  
285 ‘warm’ phase, which results from a strengthening of the subpolar gyre in response to a  
286 deepening of the Aleutian Low due to stochastic fluctuations (Wills *et al.*, 2019). The  
287 gyre strengthening thus acts to dampen temperature changes in the high-latitudes over  
288 glacial-interglacial cycles.

289

290 The glacial increase in wind stress curl seen within the model ensemble would  
291 drive a large increase in Ekman suction within the subpolar gyre (Gray *et al.*, 2018).  
292 Given the close association of the wind stress curl changes driving the expansion and  
293 strengthening of the subpolar gyre, we suggest that the proxy evidence for a  $\sim 3^\circ$   
294 southward shift in the gyre boundary is also indirect evidence for a glacial increase in  
295 Ekman suction within the subpolar gyre. The impact of this increased Ekman suction  
296 on surface ocean nutrients and CO<sub>2</sub> over deglaciation is discussed in detail in Gray *et al.*  
297 *et al.*, 2018. Increased Ekman suction would also increase the salinity of the SPG with  
298 increased upwelling of salty subsurface waters (e.g. Warren, 1983). Furthermore, both  
299 the strengthening of the gyre circulation (via increased eddy transport from the salty

300 STG gyre and the reduced residence time of water in the SPG; Emile-Geay *et al.*, 2003)  
301 and the reorganisation of the atmosphere (lower precipitation in the SPG due to the  
302 southward shift in the jet stream and atmospheric river events e.g. Laine *et al.* 2009;  
303 Lora *et al.*, 2017) would increase the salinity of the SPG. The reorganisation of the  
304 atmosphere and gyre circulation in response to ice sheet forcing may therefore play an  
305 important role in pre-conditioning basin for the enhanced overturning circulation  
306 observed within the North Pacific during glacial periods (e.g. Keigwin, 1998;  
307 Matsumoto *et al.*, 2002; Knudson and Ravelo, 2015; Max *et al.*, 2017), and points  
308 towards a weakening of the North Pacific halocline, rather than a strengthening, under  
309 glacial climates (c.f. Haug *et al.*, 1999).

310

### 311 *3.3 Deglaciation*

312         Considering all of the  $\delta^{18}\text{O}$  data from east and west of  $180^\circ$  together, our  
313 reconstruction shows the gyre boundary begins to migrate northward beginning at  $\sim 17$ -  
314 16 ka, during Heinrich Stadial 1 (HS1) (Fig. 5d). The boundary then appears relatively  
315 constant during the Bølling-Allerød (14.8-12.9 ka; B/A) with a second major shift north  
316 at  $\sim 12$  ka, during the latter part of the Younger Dryas. There is reasonable agreement  
317 between the timing of the gyre migration in the data and the deglacial model runs, which  
318 show the majority of the change occurring between  $\sim 16.5$ -12 ka (Fig. 5e); however, the  
319 model shows a steady change, rather than the two-step change in the data. We speculate  
320 this is a due to the lack of routed freshwater into the North Atlantic within these model  
321 runs, via its effects on hemispheric temperature asymmetry through heat transport. The  
322 timing also agrees with evidence of lake level changes in western North America (Fig.  
323 5c; see below) and other Pacific-wide changes in atmospheric circulation during the  
324 deglaciation (Russell *et al.*, 2014; McGee *et al.*, 2014; Jones *et al.*, 2018).

325

326           However, assessing the  $\delta^{18}\text{O}$  data from the east and west of the basin separately  
327 reveals a large difference in timing; the majority of the change occurs earlier in the  
328 deglaciation in the east of the basin ( $\sim 16.5\text{-}14$  ka) whereas the majority of the change  
329 occurs later in the deglaciation in the west of the basin ( $\sim 12.5 - 10.5$  ka). This east-west  
330 difference in timing can be seen in the raw  $\delta^{18}\text{O}_{\text{calcite}}$  data (Figure 1) and is too large to  
331 be explained by age model uncertainty. Contrary to the data, HadCM3 shows no  
332 difference in the timing of the northward shift of the gyre boundary between the east  
333 and west, although the weakening of the westerlies does occur substantially later in the  
334 west of the basin (compared to the east) within the model (Fig. 5g).

335

336           The northward migration of the gyre boundary in the east of the basin beginning  
337 at  $\sim 16.5$  ka indicates the westerly winds in the east of the basin began to shift northward  
338 at this time, concomitant with the recession of the Laurentide Ice Sheet (Lambeck *et al.*  
339 *et al.*, 2014). Such a change in atmospheric circulation within the east of the basin at this  
340 time is in good agreement with records of hydroclimate in southwestern North America  
341 (Figure 5c; Bartlein *et al.*, 1998; Lyle *et al.*, 2012; Ibarra *et al.*, 2014; McGee *et al.*,  
342 2015; Oviatt, 2015; Lora *et al.*, 2016; Shuman & Serravezza, 2017; Bhattacharya *et al.*,  
343 2018; McGee *et al.*, 2018), and suggests a clear role for dynamics in driving the  
344 observed changes in hydroclimate. However, given Sverdrup balance, changes in wind  
345 stress curl within the east of the basin should propagate across the basin and drive  
346 changes in the position of the gyre boundary in the west, and, as noted above, only a  
347 small change is seen in the west of the basin at this time.

348

349           One possible dynamical explanation for the observed difference in the timing  
350 between the east and west of the basin is that the jet stream became less zonal (i.e. more  
351 tilted) during this period, and as such, the northward shift in the westerlies in the east  
352 did not result in a substantial change to the integrated wind stress curl across the basin,  
353 resulting in a less zonal (i.e. more tilted) gyre. A more tilted jet stream does not seem  
354 unreasonable given the large changes in the size of the North American ice sheets  
355 beginning at this time (e.g. Lambeck *et al.*, 2014), and is in good agreement with  
356 terrestrial proxy records and paleoclimatic simulations of this time period (Wong *et al.*,  
357 2016; Lora *et al.*, 2016). Increased heat transport from a more tilted gyre could help  
358 explain the anomalous warmth of the SPG during the Bølling-Allerød (e.g. Gray *et al.*,  
359 2018), and may help drive wider northern-hemisphere warming at this time. We note  
360 that the tilt of the gyre in the modern North Atlantic is poorly simulated by climate  
361 models (Zappa *et al.*, 2013), and thus it may also be poorly simulated in the North  
362 Pacific. We also note the other models (besides HadCM3) better simulate the larger  
363 gyre boundary shift in the east relative to the west under glacial forcing (Fig. 4c), and  
364 thus may better simulate gyre tilt.

365

## 366 **6. Conclusions**

367           Using a basin wide compilation of planktic foraminiferal  $\delta^{18}\text{O}$  data we show  
368 that the boundary between the North Pacific subpolar and subtropical gyres shifted  
369 southward by  $\sim 3^\circ$  during the Last Glacial Maximum, consistent with sea surface  
370 temperature and productivity proxy data. This expansion of the North Pacific subpolar  
371 gyre is evident within all PMIP3 climate models forced with glacial boundary  
372 conditions. The models suggest that this expansion is associated with a substantial  
373 strengthening of the subpolar gyre. The strengthening of the subpolar gyre is driven by

374 an increase in wind stress curl within the subpolar gyre resulting from a southward shift  
375 and strengthening of the mid-latitude westerlies in the east of the basin, and a southward  
376 shift in the polar easterlies across the basin. The expansion of the gyre is driven by a  
377 southward expansion of the area of positive wind stress curl within the east of the basin,  
378 due to the southward shift in the westerlies. Using model runs with individual forcings,  
379 we demonstrate that the changes in wind stress curl and associated expansion and  
380 strengthening of the subpolar gyre are a response to the combined effects of ice sheet  
381 albedo, ice sheet topography, and CO<sub>2</sub>. Changes are small in climate model simulations  
382 where albedo and topography are forced separately, compared to their combined  
383 effects, illustrating the highly non-linear nature of the response of atmospheric  
384 circulation to ice sheet forcing (e.g. Löffverström *et al.*, 2014; Roberts *et al.*, 2019).

385

386         The southward expansion of the subpolar gyre would have brought nutrient-rich  
387 waters further south, explaining why productivity increased in the transition zone  
388 between the gyres while decreasing throughout the subpolar gyre during LGM. The  
389 expansion and contraction of the subpolar gyre acts as a mechanism to amplify  
390 temperature changes in the mid-latitudes over glacial-interglacial cycles. On the  
391 contrary, the strengthening of the subpolar gyre would increase poleward heat transport,  
392 warming the north of the basin and dampening temperature changes in the high-  
393 latitudes over glacial-interglacial cycles. The strengthening of the gyre circulation, in  
394 conjunction with increased Ekman suction (Gray *et al.*, 2018), and reduced  
395 precipitation (Lora *et al.*, 2017), would also make the subpolar gyre saltier, weakening  
396 the halocline under glacial climates (c.f. Haug *et al.*, 1999).

397

398 Our gyre-boundary reconstruction offers a constraint on the position of the mid-  
399 latitude westerly winds over the last deglaciation and suggests the westerly winds began  
400 to shift northward at ~17-16 ka, during Heinrich Stadial 1, as the Laurentide Ice Sheet  
401 receded. This reorganisation of atmospheric circulation likely drove the large changes  
402 in hydroclimate within southwestern North America (e.g. Lora *et al.*, 2016), and may  
403 be related to other changes in atmospheric circulation seen at this time across the whole  
404 Pacific, deep into the tropics and the Southern Hemisphere (e.g. D’Agostino *et al.*,  
405 2017; Jones *et al.*, 2018).

406

#### 407 **Acknowledgments**

408 We are grateful to Lloyd Keigwin for imparting the wisdom ‘If the signal is big enough,  
409 you’ll see it in the  $\delta^{18}\text{O}$  of calcite’. We acknowledge the World Climate Research  
410 Programme’s Working Group on Coupled Modelling for the coordination of CMIP and  
411 thank the climate modelling groups for producing and making available their model  
412 output (<https://esgf-node.llnl.gov/search/cmip5/>). Insightful and constructive  
413 comments from two anonymous reviewers very much improved a previous version of  
414 this manuscript. WRG, JWBR and AB were funded Natural Environment Research  
415 Council (NERC) grant NE/N011716/1 awarded to JWBR and AB. RCJW was funded  
416 by the Tamaki Foundation, NASA (Grant NNX17AH56G), and NSF (Grant AGS-  
417 1929775). RFI was funded by a NERC Independent Research Fellowship  
418 NE/K008536/1. The planktic foraminiferal  $\delta^{18}\text{O}$  compilation used in this study will be  
419 available on Pangea.

420

#### 421 **References**

422 Bartlein, P.J., Anderson, K.H., Anderson, P.M., Edwards, M.E., Mock, C.J.,  
423 Thompson, R.S., Webb, R.S., Webb, T., Whitlock, C., 1998. Paleoclimate  
424 simulations for North America over the past 21,000 years; features of the simulated

425 climate and comparisons with paleoenvironmental data. *Quaternary Science*  
426 *Reviews* 17, 549-585.

427 Boyer, T.P., Antonov, J.I., Baranova, O.K., Coleman, C., Garcia, H.E., Grodsky, A.,  
428 John-son, D.R., Locarnini, R.A., Mishonov, A.V., O'Brien, T.D., Paver, C.R.,  
429 Reagan, J.R., Seidov, D., Smolyar, I.V., Zweng, M.M., 2013. World Ocean Database  
430 2013. In: Levitus, Sydney (Ed.), Alexey Mishonov (Technical Ed.), NOAA Atlas  
431 NESDIS, vol. 72. 209 pp.

432 Braconnot, P., Harrison, S.P., Kageyama, M., Bartlein, P.J., Masson-Delmotte, V.,  
433 Abe-Ouchi, A., Otto-Bliesner, B. and Zhao, Y., 2012. Evaluation of climate models  
434 using palaeoclimatic data. *Nature Climate Change*, 2(6), 417-424.

435 Broccoli, A.J., Manabe, S., 1987. The influence of continental ice, atmospheric CO<sub>2</sub>,  
436 and land albedo on the climate of the last glacial maximum. *Climate Dynamics* 1,  
437 87-99.

438 D'Agostino, R., P. Lionello, O. Adam, and T. Schneider (2017), Factors controlling  
439 Hadley circulation changes from the Last Glacial Maximum to the end of the 21st  
440 century. *Geophysical Research Letters* 44, 8585-8591. doi:10.1002/2017GL074533.

441 Deser, C., Alexanders, M. A., Timlin, M. S., 1999. Evidence for a Wind-Driven  
442 Intensification of the Kuroshio Current Extension from the 1970s to the 1980s.  
443 *Journal of Climate* 12, 1697-1706.

444 Emile-Geay, J., Cane, M.A., Naik, N., Seager, R., Clement, A.C., van Geen, A. (2003)  
445 Warren revisited: Atmospheric freshwater fluxes and 'Why is no deep water formed  
446 in the North Pacific'. *Journal of Geophysical Research* 108,  
447 doi:10.1029/2001JC001058.

448 Forget, G, Ferreira, D, 2019. Global ocean heat transport dominated by heat export  
449 from the tropical Pacific. *Nature Geoscience*, [https://doi.org/10.1038/s41561-019-](https://doi.org/10.1038/s41561-019-0333-7)  
450 0333-7,

451 Gray, W.R., Rae, J.W.B, Wills, R.C.J., Shevenell, A.E., Taylor, B., Burke, A., Foster,  
452 G.L., Lear, C.H., 2018. Deglacial upwelling, productivity and CO<sub>2</sub> outgassing in the  
453 North Pacific Ocean. *Nature Geoscience* 11, 340–344.

454 Haug, G.H., Sigman, D.M., Tiedemann, R., Pedersen, T.F., Sarnthein M., 1999. Onset  
455 of permanent stratification in the subarctic Pacific Ocean. *Nature* 40, 779-782.

456 Huatala, S.L., Roemmich, D.H., Schmitz, W.J., 1994. Is the North Pacific in Sverdrup  
457 balance along 24°N? *Journal of Geophysical Research* 99, 16041-16052.

458 Ibarra, D. E., A. E. Egger, K. L. Weaver, C. R. Harris, and K. Maher, 2014: Rise and  
459 fall of late Pleistocene pluvial lakes in response to reduced evaporation and  
460 precipitation: Evidence from Lake Surprise, California. *Geol. Soc. Amer. Bull.*, 126,  
461 1387–1415, <https://doi.org/10.1130/B31014.1>.

462 Ivanovic, R.F., Gregoire, L.J., Kageyama, M., Roche, D.M., Valdes, P.J., Burke, A.,  
463 Drummond, R., Peltier, W.R., Tarasov, L., 2016. Transient climate simulations of  
464 the deglaciation 21–9 thousand years before present (version 1) PMIP4 Core  
465 experiment design and boundary conditions. *Geosci. Model Dev.* 9, 25632587.  
466 <https://doi.org/10.5194/gmd-9-2563-2016>.

467 Jones, T.R., Roberts, W.H.G., Steig, E.J., Cuffey, K.M., Markle, B.R., White, J.W.C  
468 (2018) Southern Hemisphere climate variability forced by Northern Hemisphere ice-  
469 sheet topography. *Nature* **554**, 351-355.

470 Keigwin, L., 1998. Glacial-age hydrography of the far northwest Pacific Ocean.  
471 *Paleoceanography* **13**, 323–339.

472 Key, R.M., Olsen, A., van Heuven, S., Lauvset, S.K., Velo, A., Lin, X., Schirnack, C.,  
473 Kozyr, A., Tanhua, T., Hoppema, M., Jutterström, S., Steinfeldt, R., Jeansson, E.,  
474 Ishi, M., Perez, F.F., Suzuki, T., 2015. Global Ocean Data Analysis Project, Version  
475 2 (GLODAPv2). ORNL/CDIAC-162, ND-P093. Carbon Dioxide Informa- tion  
476 Analysis Center, Oak Ridge National Laboratory, US Department of Energy, Oak  
477 Ridge, Tennessee. [https://doi.org/10.3334/CDIAC/OTG.NDP093\\_GLODAPv2](https://doi.org/10.3334/CDIAC/OTG.NDP093_GLODAPv2).  
478 [http://cdiac.ornl.gov/oceans/GLODAPv2/NDP\\_093.pdf](http://cdiac.ornl.gov/oceans/GLODAPv2/NDP_093.pdf).

479 Kim, S. and O’Neil, J. (1997). Equilibrium and nonequilibrium oxygen isotope effects  
480 in synthetic carbonates. *Geochimica et Cosmochimica Acta* **61**, 3461–3475.

481 Kirby, M. E., S. J. Feakins, N. Bonuso, J. M. Fantozzi, and C. A. Hiner, 2013. Latest  
482 Pleistocene to Holocene hydroclimates from Lake Elsinore, California, *Quat. Sci.*  
483 *Rev.*, 76, 1–15.

484 Knudson, K. P. and Ravelo, A. C., 2015. North Pacific Intermediate Water  
485 circulation enhanced by the closure of the Bering Strait. *Paleoceanography* **30**,  
486 PA002840.

487 Kohfeld, K. E. & Chase, Z., 2011. Controls on deglacial changes in biogenic fluxes in  
488 the North Pacific Ocean. *Quat. Sci. Rev.* **30**, 3350–3363.

489 Lambeck, K., Rouby, H., Purcell, A., Sun, Y., Sambridge, M., 2014. Sea level and  
490 global ice volumes from the Last Glacial Maximum to the Holocene. *Proc. Natl*  
491 *Acad. Sci. USA* **111**, 15296–15303.

492 LeGrande, A.N., Schmidt, G.A., 2006. Global gridded data set of the oxygen isotopic  
493 composition in seawater. *Geophys. Res. Lett.* **33**, L12604.

494 Li, C., Battisti, D.S., 2008. Reduced Atlantic Storminess during Last Glacial  
495 Maximum: Evidence from a Coupled Climate Model. *Journal of Climate* **21** 3561-  
496 3579. DOI: 10.1175/2007JCLI2166.1.

497 Lora, J. M., J. L. Mitchell, Tripathi, A. E., 2016. Abrupt reorganization of North Pacific  
498 and western North American climate during the last deglaciation, *Geophys. Res.*  
499 *Lett.*, 43, 11,796–11,804, doi:10.1002/2016GL071244.

500 Lora, J. M., 2018. Components and Mechanisms of Hydrologic Cycle Changes over  
501 North America at the Last Glacial Maximum. *Journal of Climate* **31**, 7035-7051.

502 Löffverström, M., R. Caballero, J. Nilsson, Kleman, J., 2014. Evolution of the large-  
503 scale atmospheric circulation in response to changing ice sheets over the last glacial  
504 cycle. *Climate of the Past* **10**, 1453-1471.

505 Lyle, M., Heusser, L., Ravelo, C., Yamamoto, M., Barron, J., Diffenbaugh, N. S.,  
506 Herbert, T., Andreasen, D., 2012. Out of the Tropics: The Pacific, Great Basin  
507 Lakes, and Late Pleistocene Water Cycle in the Western United States. *Science*, **337**,  
508 1629-1633.

509 Lynch-Stieglitz, J., Curry, W.B., Slowey, N. (1999) Weaker Gulf Stream in the Florida  
510 Straits during the Last Glacial Maximum. *Nature* **402**, 644-648.



511 Manabe, S., Broccoli, A.J., 1985. The influence of Continental Ice Sheets on the  
512 Climate of an Ice Age. *Journal of Geophysical Research* 90, 2167-2190.

513 Marcott, S.A. *et al.*, 2014. Centennial-scale changes in the global carbon cycle during  
514 the last deglaciation. *Nature* **514**, 617-619. doi:10.1038/nature13799

515 Matsumoto, K., Oba, T. & Lynch-Stieglitz, J., 2002. Interior hydrography and  
516 circulation of the glacial Pacific Ocean. *Quat. Sci. Rev.* **21**,1693–1704.

517 Max, L., Rippert, N., Lembke-Jene, L., Mackensen, A., Nürnberg, D., Tiedemann, R.,  
518 2017. Evidence for enhanced convection of North Pacific Intermediate Water to the  
519 low-latitude Pacific under glacial conditions. *Paleoceanography* **32**, 41–55.

520 McGee, D., Quade, J., Edwards, R.L, Broecker, W.S., Cheng, H., Reiners, P.W.,  
521 Evenson, N., 2012. Lacustrine cave carbonates: Novel archives of paleohydrologic  
522 change in the Bonneville Basin (Utah, USA). *Earth and Planetary Science Letters*  
523 **351-352**, 182-194.

524 McGee, D., Donohoe, A., Marshall, J., Ferreira, D. (2014) Changes in ITCZ location  
525 and cross-equatorial heat transport at the Last Glacial Maximum, Heinrich Stadial  
526 1, and the mid-Holocene. *Earth and Planetary Science Letters* **390**, 69-79.

527 McGee, D., Moreno-Chamarro, E., Marshall, J., Galbraith, E.D. (2018) Western U.S.  
528 lake expansions during Heinrich stadials linked to Pacific Hadley circulation.  
529 *Science Advances* 4, eaav0118.

530 Morris, P.J., Swindles, G.T., Valdes, P.J., Ivanovic, R.F., Gregoire, L.J., Smith, M.W.,  
531 Tarasov, L., Haywood, A.M., Bacon, K.L., 2018. Global peatland initiation driven  
532 by regionally asynchronous warming. *PNAS* 201717838.  
533 <https://doi.org/10.1073/pnas.1717838115>.

534 Nelson, S.T., Wood, M.J., Mayo, A.L., Tingey, D.G., Eggett, D., 2005. Shoreline tufa  
535 and tufaglomerate from Pleistocene Lake Bonneville, Utah, USA: stable isotopic  
536 and mineralogical records of lake conditions, processes, and climate. *Journal of*  
537 *Quaternary Science* **20**, 3–19.

538 Okazaki, Y., Timmermann, A., Menviel, L., Harada, N., Abe-Ouchi, A., Chikamoto,  
539 M., Mouchet, A., and Asahi, H., 2010. Deepwater Formation in the North Pacific  
540 During the Last Glacial Termination. *Science* **329**, 200-204.

541 Oster, J.L., Ibarra, D.E., Winnick, M.J., Maher, K., 2015. Steering of westerly storms  
542 over western North America at the Last Glacial Maximum. *Nature Geoscience* **8**,  
543 201-205.

544 Oviatt, C. G., R. S. Thompson, D. S. Kaufman, J. Bright, and R. M. Forester, 1999.  
545 Reinterpretation of the Burmester Core, Bonneville Basin, Utah, *Quat. Res.*, 52,  
546 180–184.

547 Oviatt, C. G., 2015. Chronology of Lake Bonneville, 30,000 to 10,000 yr B.P.  
548 *Quaternary Science Reviews* 110, 166-171.

549 Pausata, F. S. R., Li, C., Wettstein, J. J., Kageyama, M., and Nisancioglu, K. H., 2011.  
550 The key role of topography in altering North Atlantic atmospheric circulation during  
551 the last glacial period, *Clim. Past* **7**, 1089-1101, [https://doi.org/10.5194/cp-7-1089-](https://doi.org/10.5194/cp-7-1089-2011)  
552 2011.

553 Rae, J. W. B., Sarnthein, M., Foster, G. L., Ridgwell, A., Grootes, P. M., and Elliott,  
554 T., 2014. Deep water formation in the North Pacific and deglacial CO<sub>2</sub> rise.  
555 *Paleoceanography* **29**, 645–667.

556 Roberts, W. H. G., Valdes, P. J., 2017. Green Mountains and White Plains: The Effect  
557 of Northern Hemisphere Ice Sheets on the Global Energy Budget. *Journal of Climate*  
558 **30**, 3887- 3905. DOI: 10.1175/JCLI-D-15-0846.1.

559 Roberts, W.H.G., Li, C., Valdes, P.J., 2019. The mechanisms that determine the  
560 response of the Northern Hemisphere’s stationary waves to North American ice  
561 sheets. *Journal of Climate*, <https://doi.org/10.1175/JCLI-D-18-0586.1>

562 Russell, J.M., Russell, Vogel, H., Konecky, B.L., Bijaksana, S., Huang, Y., Melles, M.,  
563 Wattrus, N., Costa, K., King, J.W., 2014. Glacial forcing of central Indonesian  
564 hydroclimate since 60,000 yr BP. *Proc. Natl Acad. Sci. USA* **111**, 5100–5105.

565 Sawada, K. and Handa, N., 1998. Variability of the path of the Kuroshio ocean current  
566 over the past 25,000 years. *Nature* **392**, 592–595.

567 Schrag, D. P., Adkins, J. F., McIntyre, K., Alexander, J. L., Hodell, D. A., Charles, C.  
568 D. McManus, J. F., 2002. The oxygen isotopic composition of seawater during the  
569 Last Glacial Maximum. *Quaternary Science Reviews* **21**, 331-342.

570 Shuman, B.N., Serravezza, M., 2017. Patterns of hydroclimatic change in the Rocky  
571 Mountains and surrounding regions since the last glacial maximum. *Quaternary*  
572 *Science Reviews* **173**, 58-77.

573 Sverdrup, 1947. Wind-Driven Currents in a Baroclinic Ocean; with Application to the  
574 Equatorial Currents of the Eastern Pacific. *PNAS* **33**, 318–26.

575 Taylor, K. E., R. J. Stouffer, and G. A. Meehl, 2012: An overview of CMIP5 and the  
576 experiment design. *Bull. Am. Meteorol. Soc.*, **93** (4), 485–498

577 Thompson and Shackleton, 1980. North Pacific palaeoceanography: late Quaternary  
578 coiling variations of planktonic foraminifer *Neogloboquadrina pachyderma*. *Nature*  
579 **287**, 829–833.

580 Warren, B.A. (1983) Why is no deep water formed in the North Pacific? *Journal of*  
581 *Marine Research* **41**, 327-347.

582 Wills, R. C. J., Battisti, D. S., Proistosescu, C., Thompson, L., Hartmann, D. L., &  
583 Armour, K. (2019). Ocean circulation signatures of North Pacific decadal  
584 variability. *Geophysical Research Letters*, **46**.  
585 <https://doi.org/10.1029/2018GL080716>

586 Wong, C. I., G. L. Potter, I. P. Montañez, B. L. Otto-Bliesner, P. Behling, and  
587 J. L. Oster (2016), Evolution of moisture transport to the western U.S. during the last  
588 deglaciation, *Geophys. Res. Lett.*, **43**, 3468–3477, doi:10.1002/2016GL068389.

589 Wood, S.N. (2011) Fast stable restricted maximum likelihood and marginal likelihood  
590 estimation of semiparametric generalized linear models. *Journal of the Royal*  
591 *Statistical Society (B)* **73**, 3-36.

592 Wood, S.N., Pya N., Säfken, B. (2016) Smoothing Parameter and Model Selection for  
593 General Smooth Models, *Journal of the American Statistical Association*, **111**:516,  
594 1548-1563, DOI: 10.1080/01621459.2016.1180986

595 Wunsch, C., 2011. The decadal mean ocean circulation and Sverdrup balance. *Journal*  
596 *of Marine Research* **69**, 417-434.

597 Zappa, G., L.C. Shaffrey, and K.I. Hodges (2013) The Ability of CMIP5 Models to  
598 Simulate North Atlantic Extratropical Cyclones. *Journal of Climate* **26**, 5379–5396,  
599 <https://doi.org/10.1175/JCLI-D-12-00501.1>

600

601

602

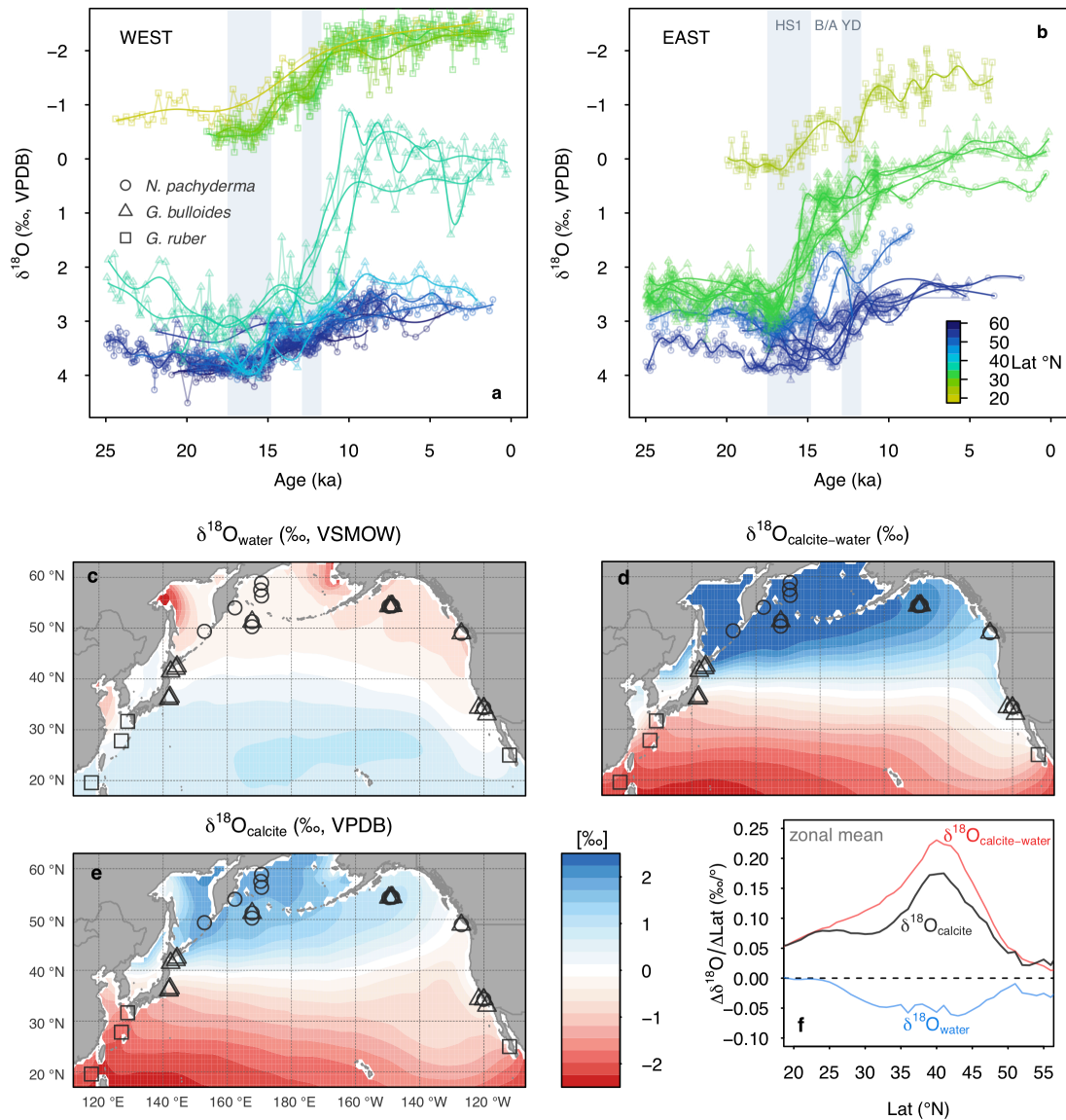
603

604

605

606

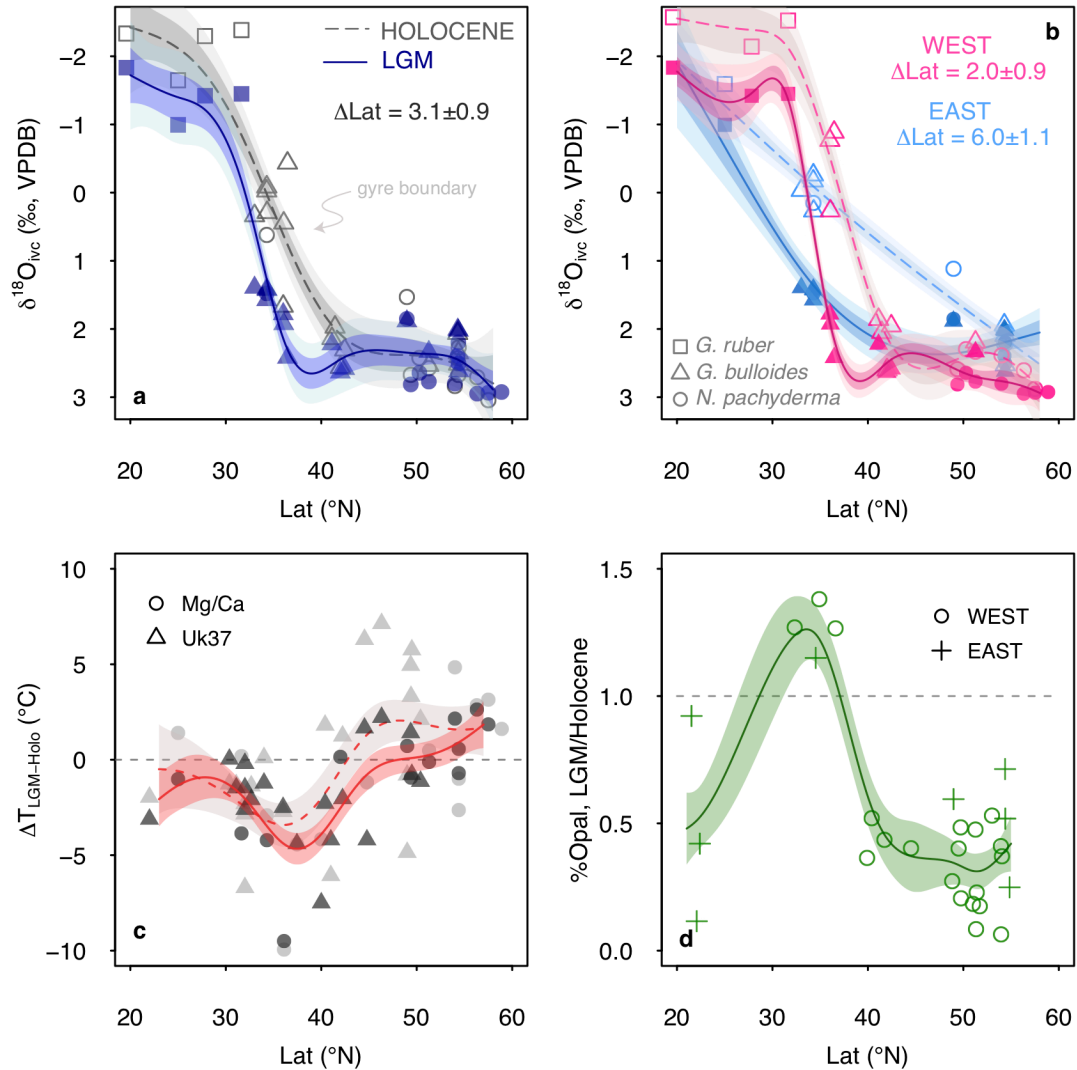
607



608

609 **Figure 1** Planktic foraminiferal  $\delta^{18}\text{O}$  versus age with core site latitude represented by colour. Data are  
 610 divided east (b) and west (a) of  $180^{\circ}$ . HS1, B/A and YD are Heinrich Stadial 1 (14.8-17.5 ka), Bølling-  
 611 Allerød (12.9-14.8 ka) and the Younger Dryas (11.8-12.9 ka), respectively. (c) gridded  $\delta^{18}\text{O}_{\text{water}}$  from  
 612 LeGrande and Schmidt (2006) (d) calcite-water fractionation calculated using WOA13 mean annual  
 613 temperature (Boyer et al., 2013) and the temperature-fractionation relationship of Kim and O'Neil  
 614 (1997) (e) predicted  $\delta^{18}\text{O}_{\text{calcite}}$  using (c) and (d) (note the colour scale is the same for all three panels)  
 615 (f) slope of the zonal-mean meridional gradient in  $\delta^{18}\text{O}_{\text{water}}$ ,  $\delta^{18}\text{O}_{\text{calcite-water}}$  and  $\delta^{18}\text{O}_{\text{calcite}}$ . The steepest  
 616 part of the meridional  $\delta^{18}\text{O}_{\text{calcite}}$  gradient is lies at the gyre boundary, and is a result of the large  
 617 temperature difference between the gyres.

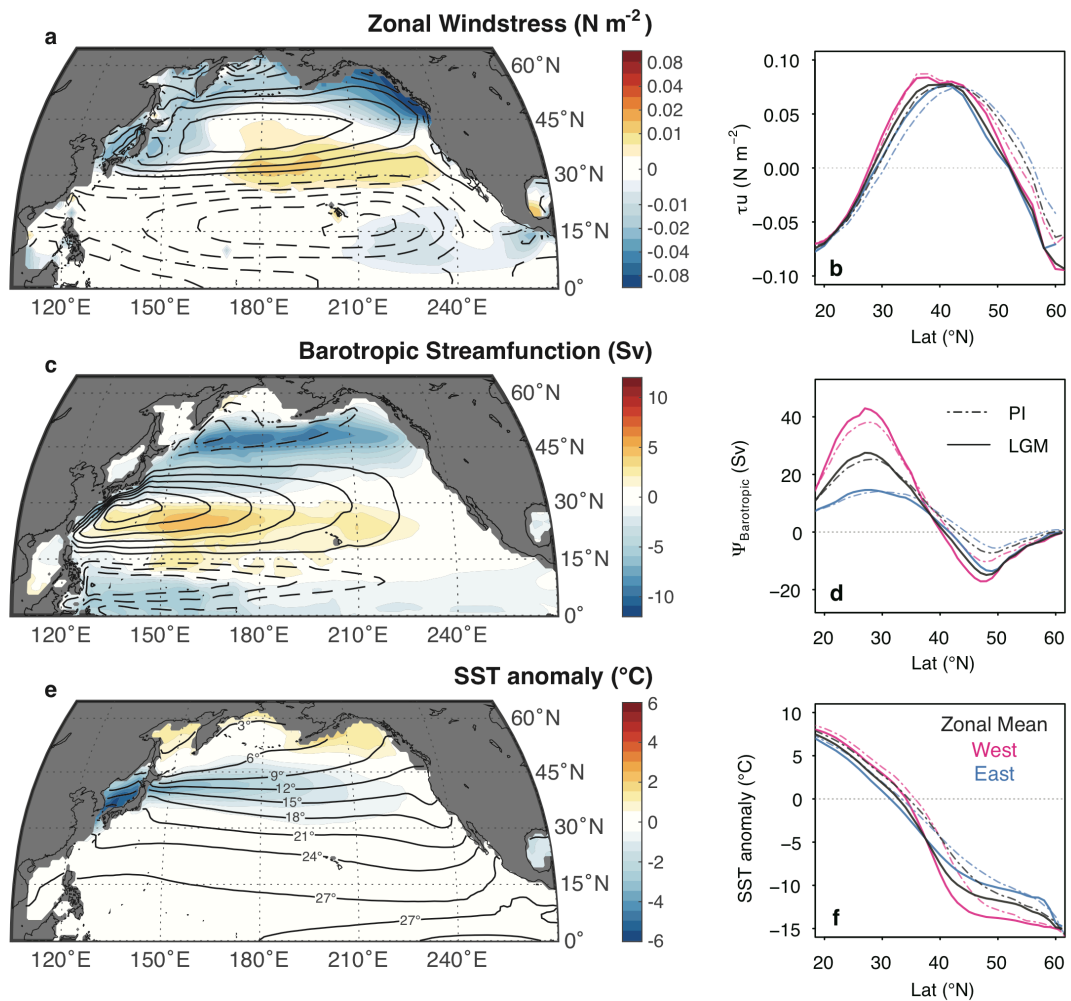
618



619

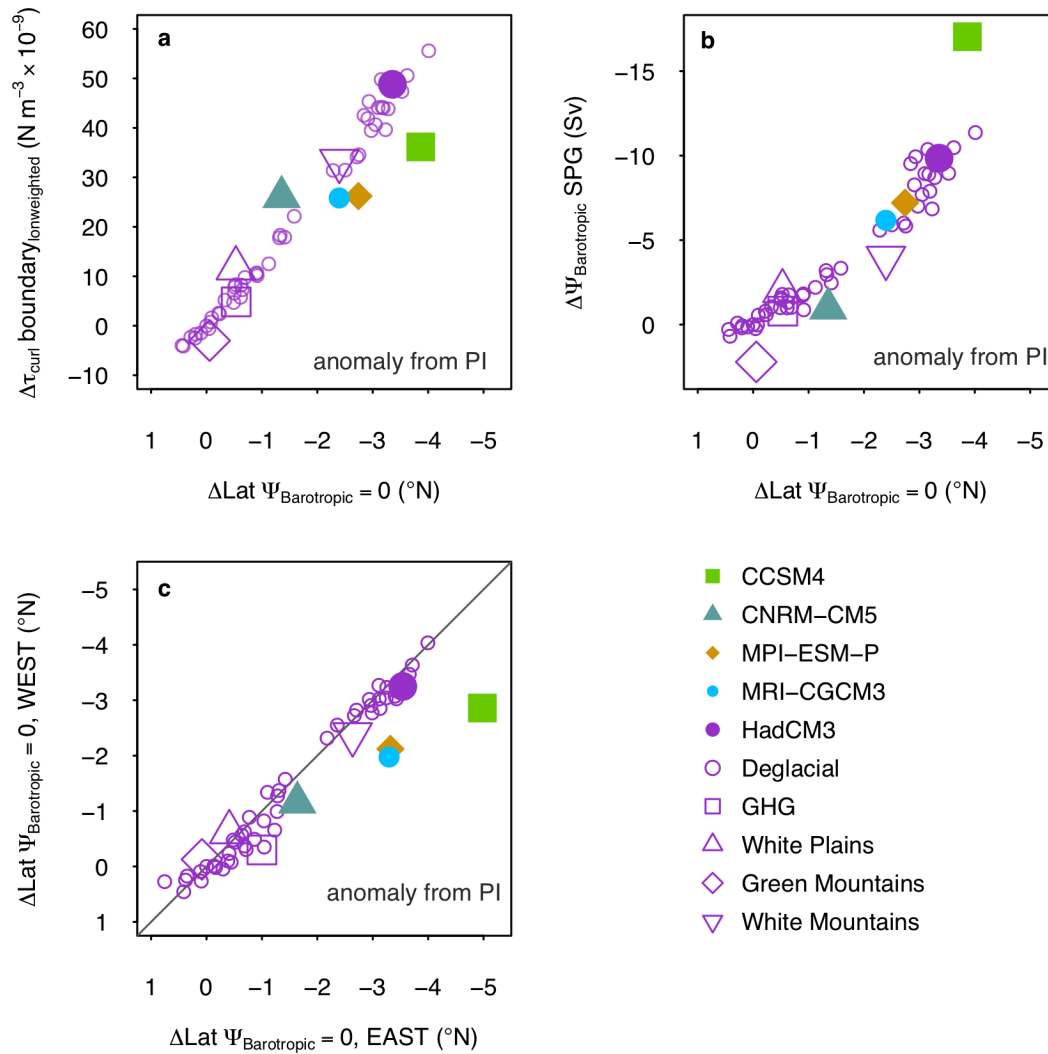
620 **Figure 2 (a)** Holocene (open symbols, dashed line) and LGM (filled symbols, solid line) foraminiferal  
 621  $\delta^{18}\text{O}$  data versus latitude – symbols reflect species of planktic foraminifera (see panel b). Foraminiferal  
 622  $\delta^{18}\text{O}$  values have been corrected for whole ocean changes in  $\delta^{18}\text{O}_{\text{water}}$  due to changes in terrestrial ice  
 623 volume and the mean ocean change in SST from the PMIP3 ensemble ( $\delta^{18}\text{O}_{\text{ivc}}$ ; see Methods). The data  
 624 are fit with a general additive model (see Methods), with the standard error (68% and 95%) of the fit  
 625 shown **(b)** as in (a), however with data separated east and west of  $180^\circ$  **(c)** Compiled LGM-Holocene  
 626 SST differences versus latitude, based on Mg/Ca and  $\text{U}^{\text{k}37}$ : Open symbols/dashed line is LGM proxy  
 627 SST minus modern climatological SST. Filled symbols/solid line is LGM proxy SST minus Holocene  
 628 proxy SST **(d)** Compiled %Opal from Kohfeld and Chase (2011) data, shown as a ratio of  
 629 LGM/Holocene versus latitude, with a value of greater than 1 indicating a glacial increase. In (c) and (d)  
 630 the data are fit with a general additive model, with the standard error of fit (68%) shown.

631



632

633 **Figure 3** PMIP3 ensemble mean of (a) LGM-PI zonal windstress ( $\tau_z$ ), with the PI climatology indicated  
 634 by contours (contour interval of  $0.04 \text{ N m}^{-2}$ ; dashed is negative and solid is positive), (b) zonal average  
 635 and averages east and west of  $180^{\circ}$  of zonal windstress in LGM and PI, (c) LGM-PI barotropic  
 636 streamfunction ( $\Psi_{\text{barotropic}}$ ), with the PI climatology indicated by contours (contour interval of  $10 \text{ Sv}$ ;  
 637 dashed is negative and solid is positive), (d) zonal average and averages east and west of  $180^{\circ}$  of the  
 638 barotropic streamfunction in LGM and PI (e) LGM-PI SST anomaly from global mean, with the PI  
 639 climatology indicated by the contours (f) zonal average and averages east and west of  $180^{\circ}$  of the SST  
 640 anomaly from global mean in the LGM and PI.



641

642 **Figure 4 (a)** LGM-PI change in latitude of zonal-mean  $\Psi_{\text{barotropic} = 0}$  versus change in longitudinally  
 643 weighted mean  $\nabla \times \tau$  ( $\tau_{\text{curl}}$ ) across the southern boundary of the subpolar gyre (38-50 °N) **(b)** LGM-PI  
 644 change in latitude of zonal mean  $\Psi_{\text{barotropic} = 0}$  versus change in  $\Psi_{\text{barotropic}}$  within the subpolar gyre  
 645 (maximum north of 40°) **(c)** LGM-PI change in latitude of zonal mean  $\Psi_{\text{barotropic} = 0}$  east and west of  
 646 180°. Green Mountains = LGM ice sheet topography with PI albedo, White Mountains = LGM ice sheet  
 647 albedo with PI topography, White Mountains = LGM ice sheet topography and albedo.

648

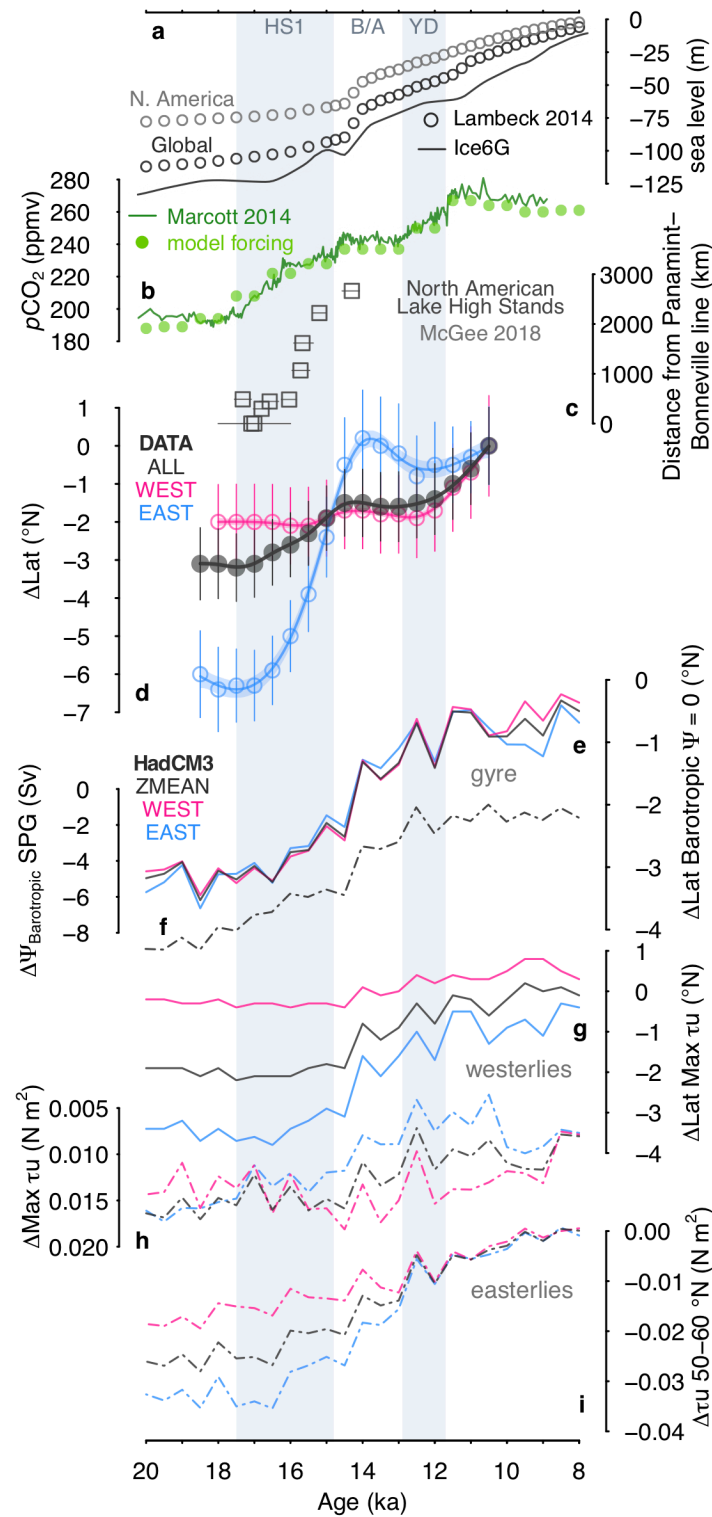
649

650

651

652

653



654

655 **Figure 5 (a)** Sealevel curve of Lambeck *et al.* (2014) and sealevel equivalent of global and  
 656 American ice sheet volume in the ICE6Gc ice sheet reconstruction **(b)** Atmospheric  $p\text{CO}_2$  record of  
 657 Marcott *et al.* (2014) and  $p\text{CO}_2$  forcing used in model **(c)** north-westward progression of lake high stands  
 658 in southwestern North America (McGee *et al.*, 2018) **(d)** reconstructed change in gyre boundary position  
 659 with  $1\sigma$  uncertainty (east and west is east and west of  $180^\circ$ ) **(e)** modelled change in gyre boundary



660 position **(f)** modelled change in subpolar gyre strength (maximum north of 40°) **(g)** modelled change in  
661 westerly position (determined as latitude of maximum zonal windstress,  $\tau_u$ ) **(h)** modelled change in  
662 westerly strength (determined as maximum  $\tau_u$ ) **(i)** modelled change in wind stress strength exerted by  
663 the easterlies (determined as mean  $\tau_u$  between 50-60 °N). For model results solid lines denote a change  
664 in position, and the dashed lines denote a change in strength. See Figure S8 for meridional profiles of  
665 **(g)**, **(h)**, and **(i)**.

666

667

668

669

670

671

672

673

674

675

676

677

678

679

680

681

682

683

684

685

686

687

688

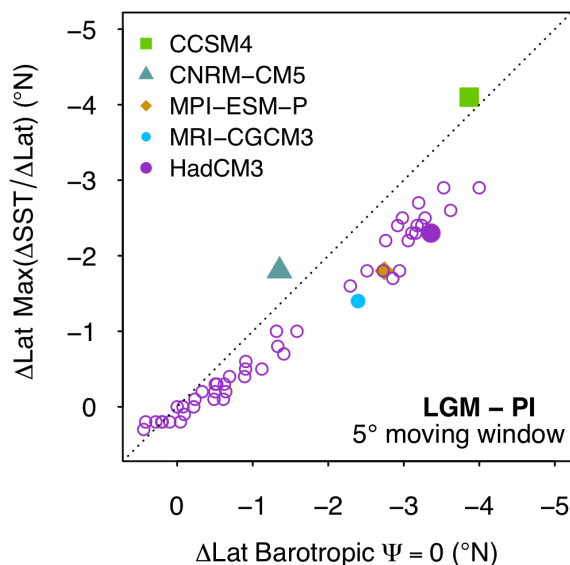
689

## *supporting information*

690

691 *Using planktic foraminiferal  $\delta^{18}\text{O}_{\text{calcite}}$  to trace the gyre boundary*

692 Our ability to use the planktic foraminiferal  $\delta^{18}\text{O}_{\text{calcite}}$  to trace the gyre boundary  
693 comes from the dominance of the temperature signal over that of  $\delta^{18}\text{O}_{\text{water}}$  in driving  
694 the meridional pattern of  $\delta^{18}\text{O}_{\text{calcite}}$  across the basin; the temperature signal is ~5 times  
695 greater than the  $\delta^{18}\text{O}_{\text{water}}$  (~salinity) signal (Figure 1). As the spatial temperature pattern  
696 across the basin is primarily governed by the gyre circulation, with the steepest  
697 meridional temperature gradient (and thus meridional  $\delta^{18}\text{O}_{\text{calcite}}$  gradient) at the gyre  
698 boundary, we can use the meridional profiles of temperature ( $\sim\delta^{18}\text{O}_{\text{calcite}}$ ) to track the  
699 movement of the gyre boundary. Coupled climate models demonstrate a very tight  
700 coupling between the LGM-PI change in latitude of gyre boundary (defined where  
701 barotropic stream function = 0) and LGM-PI change in the latitude of maximum  
702 latitudinal gradient in sea surface temperature (SST) (Figure S1). As no mechanism  
703 exists to drive changes in  $\delta^{18}\text{O}_{\text{water}}$  of the same magnitude as the changes in  $\delta^{18}\text{O}_{\text{calcite-}}$   
704 <sub>water</sub> fractionation from the large temperature difference between the gyres (Figure 1d),  
705 the temperature signal will always dominate over the  $\delta^{18}\text{O}_{\text{water}}$  signal in determining the  
706 spatial pattern of  $\delta^{18}\text{O}_{\text{calcite}}$  (Figure 1e) across the basin and the maximum meridional  
707  $\delta^{18}\text{O}_{\text{calcite}}$  gradient (Figure 1f); thus, while there are likely to be local changes in  $\delta^{18}\text{O}_{\text{water}}$   
708 across the basin, the steepest part of the meridional  $\delta^{18}\text{O}_{\text{calcite}}$  gradient will always be  
709 determined by temperature, allowing us to use meridional profiles of  $\delta^{18}\text{O}_{\text{calcite}}$  to track  
710 the position of the gyre boundary through time.



711

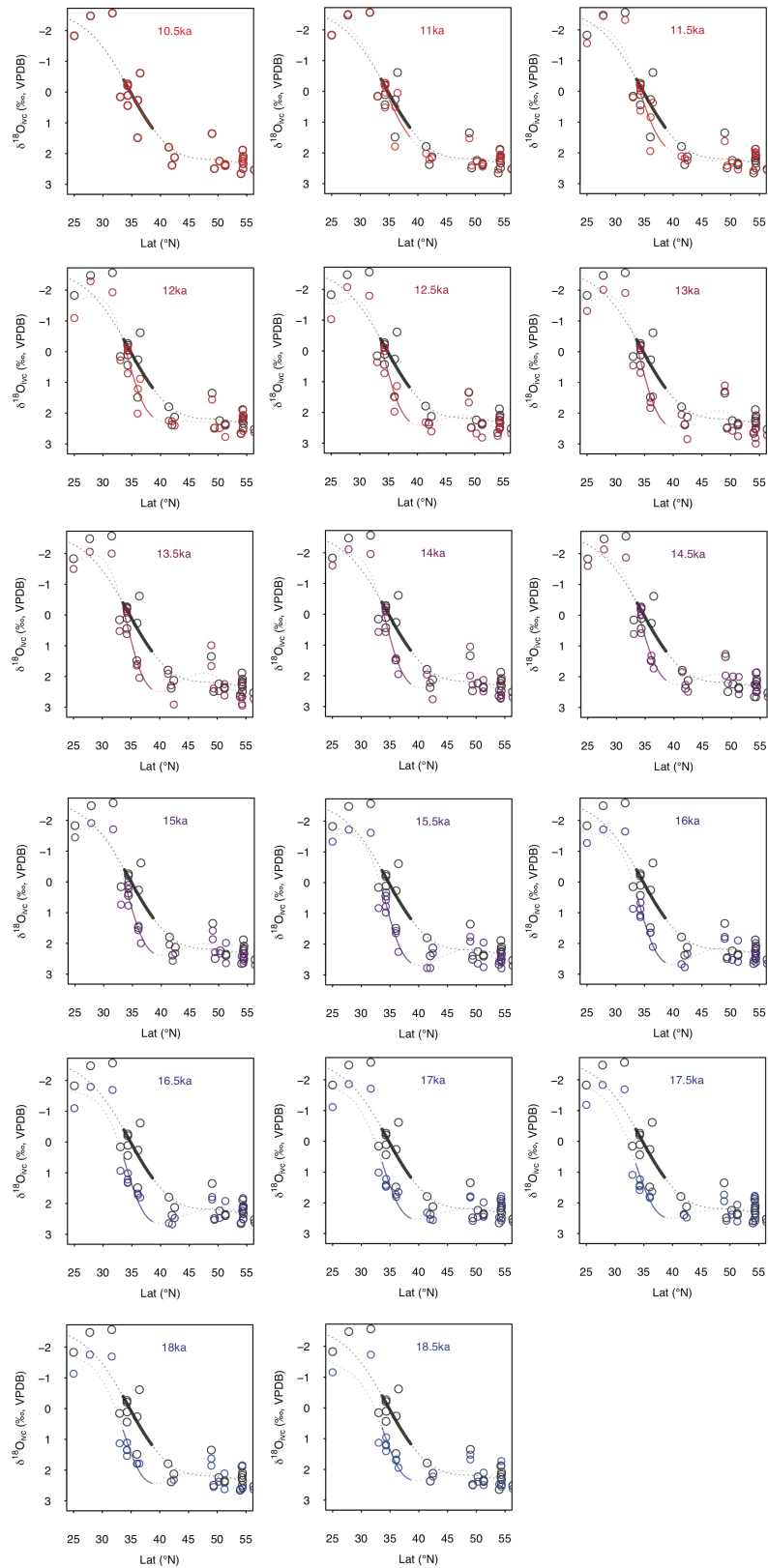
712 **Figure S1** Modelled zonal mean LGM-pre-industrial (PI) change in latitude of gyre boundary (defined  
 713 where barotropic stream function = 0) versus LGM-PI change in latitude of maximum meridional  
 714 gradient in sea surface temperature (SST) within a 5° moving window; the close relationship  
 715 demonstrates past changes in the position of the maximum gradient in SST/Lat (and thus  $\sim\delta^{18}\text{O}_{\text{calcite}}/\text{Lat}$ )  
 716 can be used to trace changes in the position of the gyre boundary.  
 717

718 We model the  $\delta^{18}\text{O}_{\text{calcite}}$  data as a function of latitude, using a general additive  
 719 model (GAM) (Wood, 2011; Wood *et al.*, 2016) in the *mgcv* package in R (R core  
 720 Team) at 500 yr timesteps from 18.5 to 10.5 ka (the time interval for which we have  
 721 sufficient spatial and temporal resolution in our dataset; Figure 1),

$$722 \quad \delta^{18}\text{O}_{\text{calcite}} = \beta + f(\text{Lat}) + \varepsilon$$

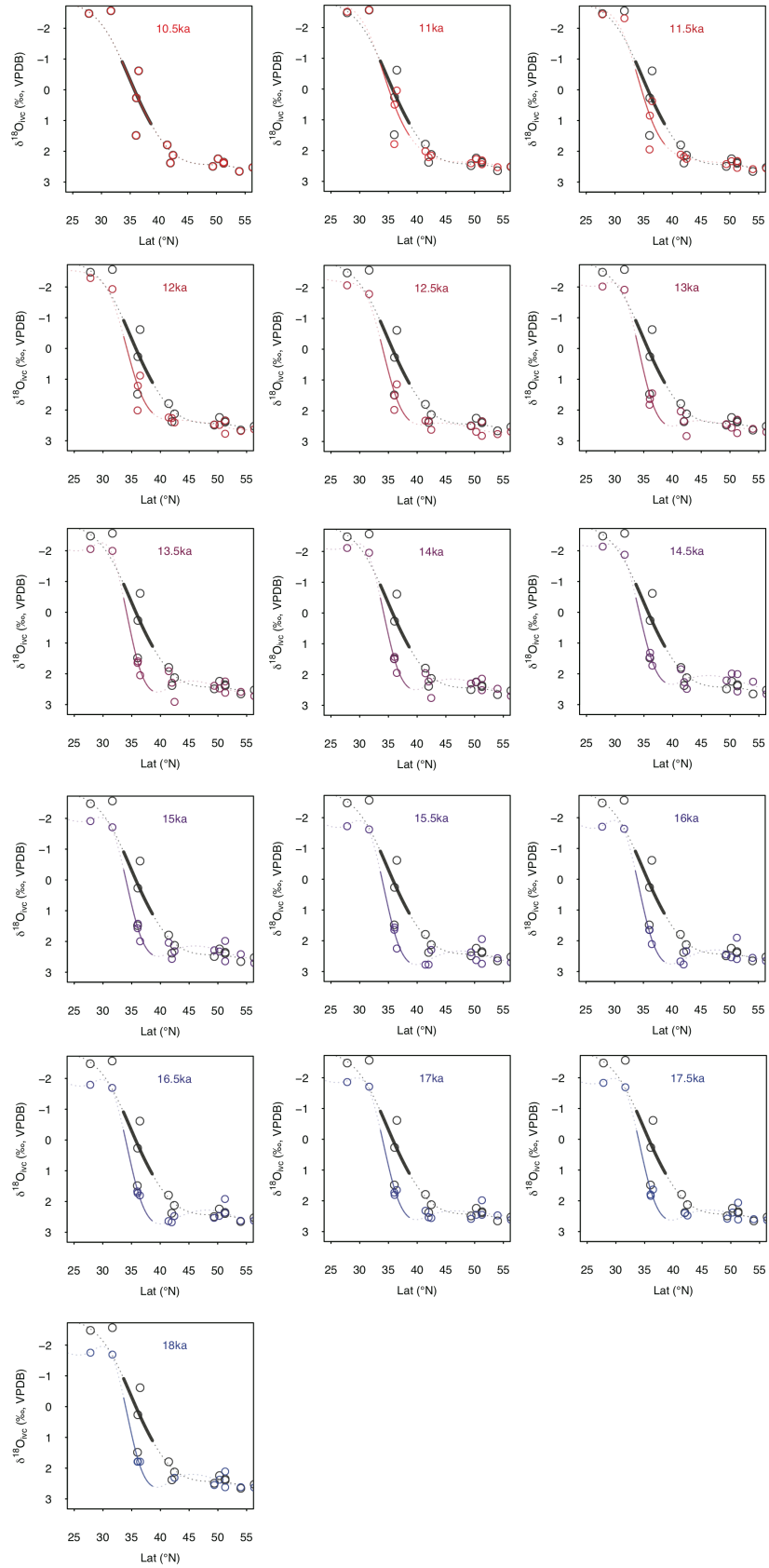
723 where  $f(\text{Lat})$  is the sum of the underlying basis functions (Wood, 2011; Wood *et al.*,  
 724 2016). The smoothing term ( $\lambda$ ) was determined using generalised cross validation  
 725 (GCV). We tested the models fitted using GCV by fitting models with an identical form,  
 726 however using Reduced Maximum Likelihood (REML), which can sometimes be a  
 727 preferable method to GCV (Reis and Ogden, 2009; Wood *et al.*, 2016), to determine  
 728 the smoothing term; both GCV and REML result in identical smoothing terms, very  
 729 similar degrees of freedom (4.06 with GCV versus 4.19 with REML), and  
 730 indistinguishable model fits.

731



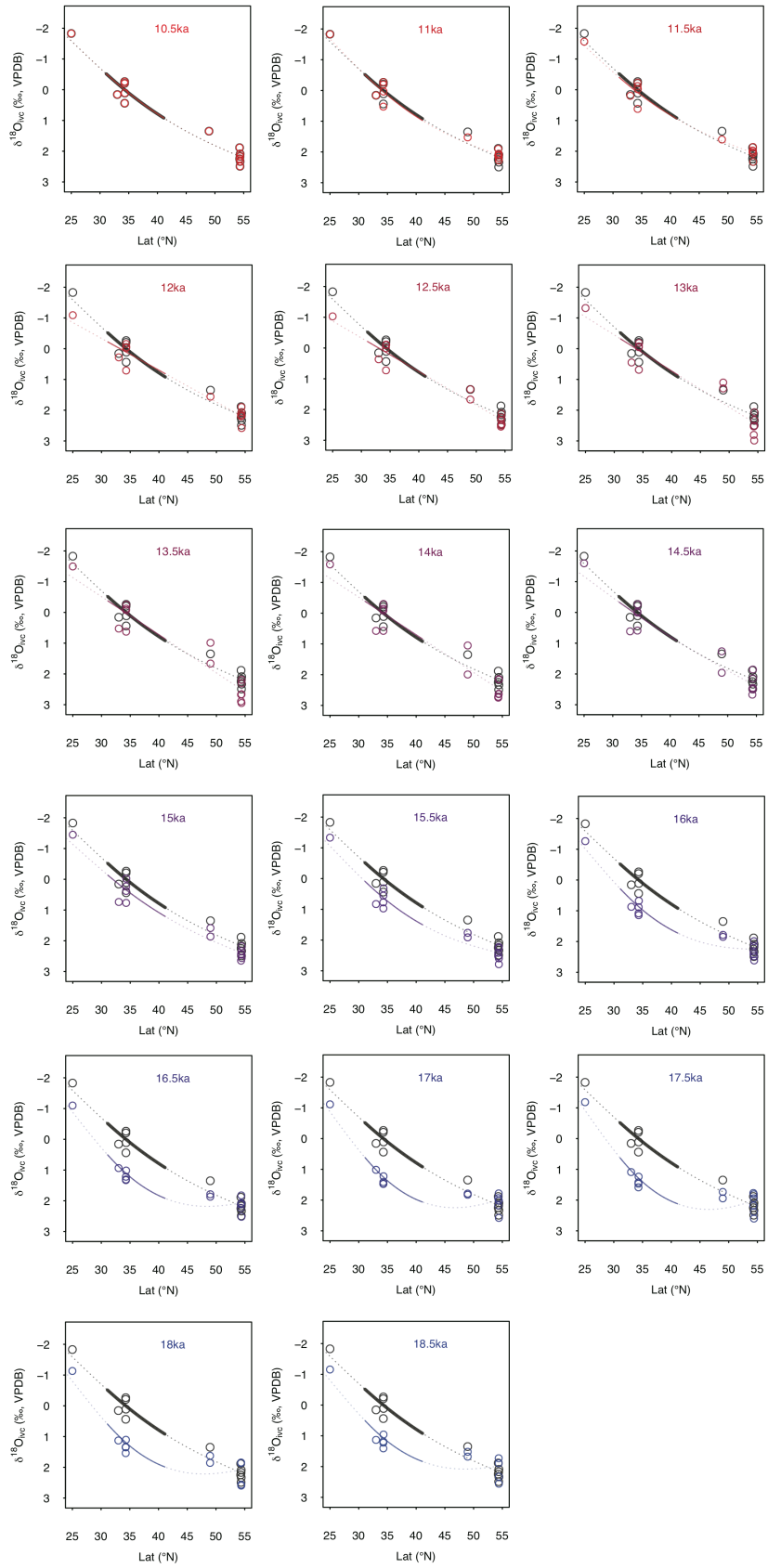
732

733 **Figure S2** GAM fits to  $\delta^{18}\text{O}_{\text{calcite}}$  data as a function of latitude at 500 year timesteps from 18.5 to 10.5 ka  
 734 (colours); the GAM fit to Holocene  $\delta^{18}\text{O}_{\text{calcite}}$  data (10.5 ka) is shown in grey. The portion of the curve  
 735 within the latitudinal band used to calculate the shift in gyre position is shown by the solid line; at each  
 736 timestep we calculate the latitudinal shift that minimises the Euclidian distance between the solid part of  
 737 the coloured curve and the solid part of the grey curve. Data are the combined east-west dataset (marked  
 738 ALL on Figure 4).



739  
740

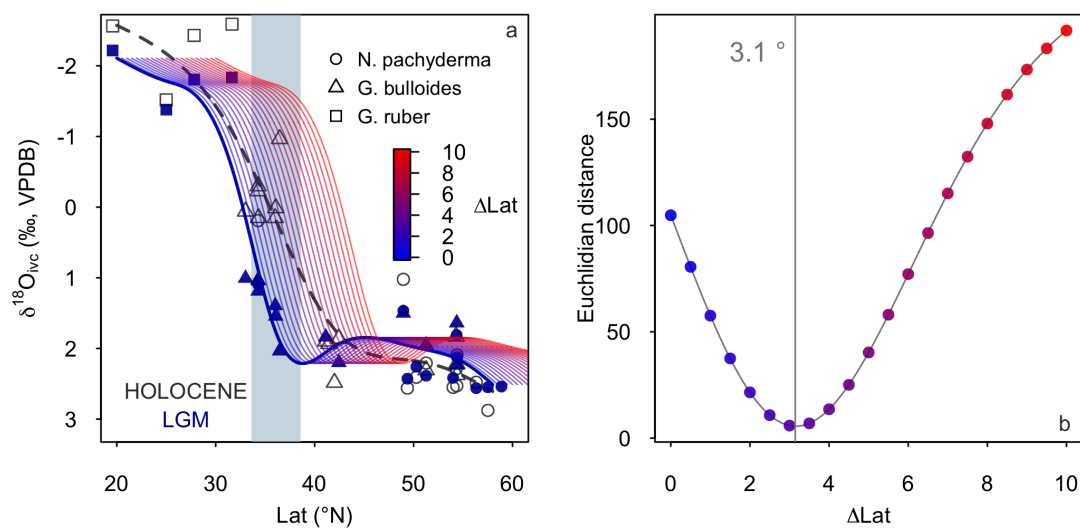
**Figure S3** As figure SX, however data are from west of 180°.



741  
742  
743

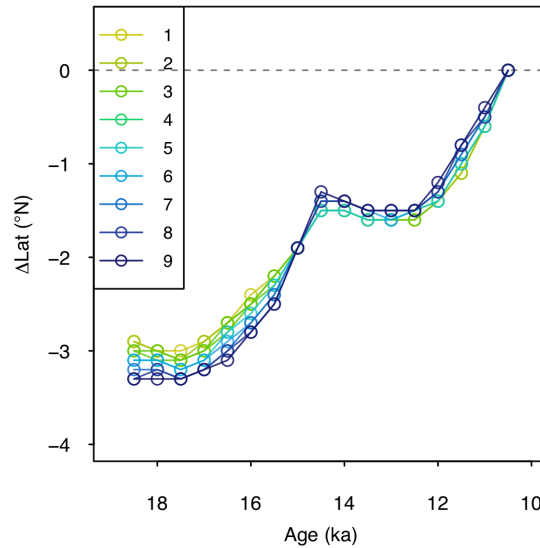
Figure S4 As figure SX, however data are from east of 180°.

744 We calculate the change in gyre boundary position over deglaciation as the  
 745 latitudinal shift ( $x^\circ$ ) that minimises the Euclidian distance ( $L^2$ ) between the Holocene  
 746 (taken as  $10.5 \pm 0.5$  ka)  $\delta^{18}\text{O}_{\text{calcite}} \sim \text{latitude}$  GAM fit and the GAM fit to each time step,  
 747 within a latitudinal band spanning the gyre boundary; this latitudinal band is centred  
 748 around the maximum gradient in  $\delta^{18}\text{O}_{\text{calcite}}$  versus latitude in the Holocene data within  
 749 a  $5^\circ$  moving window ( $36.1^\circ\text{N}$ ). In the combined dataset from the east and west, and  
 750 the data from the west only, we calculate the latitudinal shift using a  $5^\circ$  latitudinal band  
 751 (i.e.  $33.6$  to  $38.6^\circ\text{N}$ ), and we note the size of this latitudinal band has only a negligible  
 752 effect on our results (Fig. SX); as the gyre boundary (and thus meridional temperature  
 753 and  $\delta^{18}\text{O}_{\text{calcite}}$  gradient) is more diffuse in the east, we use a slightly larger window of  
 754  $10^\circ$  (i.e.  $31.1$  to  $41.1^\circ\text{N}$ ).



755

756 **Figure S5** method used to calculate the shift in gyre boundary position **(a)** at each time step (here LGM,  
 757 18.5 ka) we calculate the gyre boundary shift as the latitudinal shift ( $x^\circ$ , in  $0.1^\circ$  increments from 0 to 10  
 758 degrees) that minimises the Euclidian distance **(b)** within a specified latitudinal band (grey box in (a))  
 759 between the GAM fit to the timestep and the Holocene in data is calculated. The coloured lines in (a)  
 760 show the LGM GAM fit shifted north in  $0.5^\circ$  increments, and the coloured dots in (b) show the Euclidian  
 761 distance at each increment, with the colour indicating the degree to which the curve has been shifted.  
 762



763

764 **Figure S6 (a)** calculated change in the position of the gyre boundary using different sizes of latitudinal  
 765 band (between 1° and 9°) in which the Euclidian distance is calculated; the size of latitudinal band (the  
 766 grey box in figure SXa above) has very little effect on the results.  
 767

768 We note that the steepest part of the Holocene curve ( $\sim 36.1^\circ\text{N}$ ) using the  
 769 combined dataset from the east and west, is further south than the zonal mean position  
 770 of the gyre boundary today ( $\sim 40^\circ\text{N}$ ). This is due to the westward bias within the dataset  
 771 (i.e. there are many more sites in the west relative to the east within the dataset), and  
 772 the gyre boundary is located slightly further south in the west relative to the zonal mean;  
 773 the maximum meridional gradient in mean annual SST is found at  $\sim 36^\circ\text{N}$  along the  
 774 western margin of the basin (Boyer et al., 2013), in good agreement with our  
 775 reconstruction.

776

777 We also note that if we use a totally different method to calculate the change in  
 778 position of the gyre boundary, simply calculating the change in latitude in the steepest  
 779 part of the meridional  $\delta^{18}\text{O}_{\text{calcite}}$  gradient (within a  $5^\circ$  moving window), we arrive at a  
 780 very similar estimate of a  $\sim 2.6^\circ$  southward shift between the Holocene and LGM. This  
 781 method is more prone to anomalous values at the latitudinal extremes, hence we opt for  
 782 the method of calculating the latitudinal shift that minimises the Euclidian distance



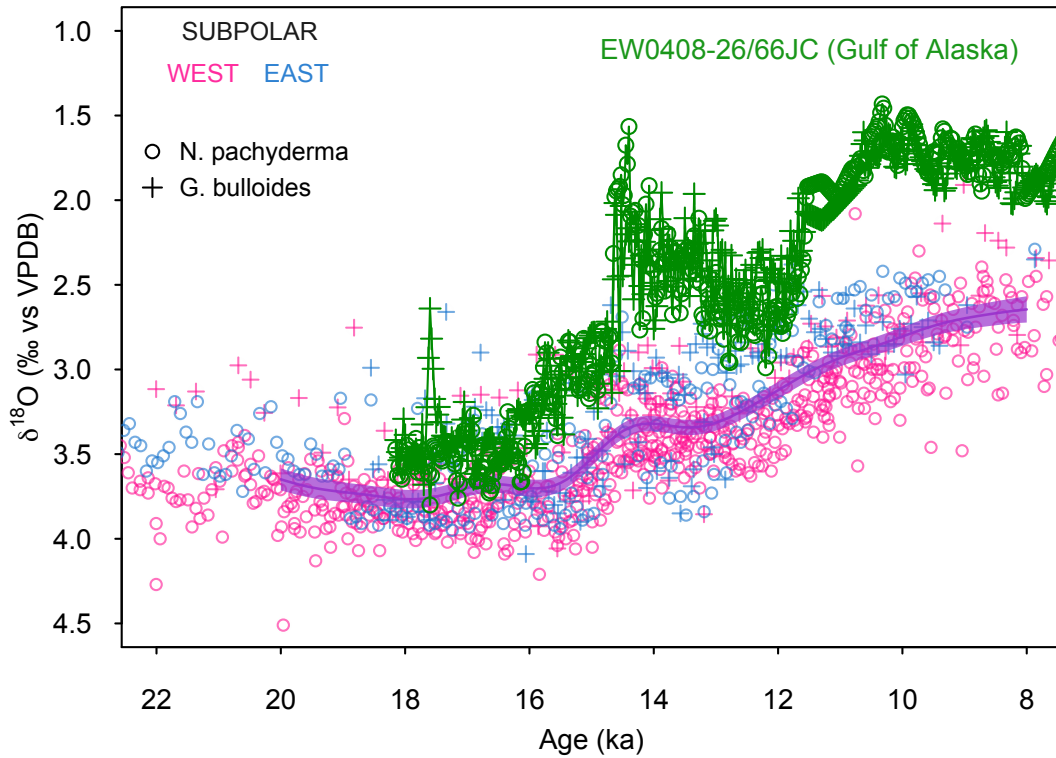
783 between timesteps within a defined latitudinal band described above; however, the  
784 agreement between the two methods is reassuring.

785

#### 786 *Planktic foraminiferal $\delta^{18}O_{\text{calcite}}$ compilation*

787 We compiled all available planktic foraminiferal calcite  $\delta^{18}O$  from cores across the  
788 North Pacific. All data were kept on the original age models, except in the case when  
789 data were only available on uncalibrated  $^{14}C$  age models, in which case the  $^{14}C$  data  
790 were recalibrated using INTCAL13 (Reimer et al., 2013) using an average of the  
791 modern reservoir age at each site and a regional glacial increase of +400 years with  
792 large uncertainties ( $\pm 500$  years). All  $\delta^{18}O_{\text{calcite}}$  data along with the core, location, water  
793 depth, species, sediment depth, age, and original data reference are given in Table S1.

794 We only include cores spanning the interval between 10.5 to 18.5 ka with an average  
795 resolution of  $>1$  point per ka. We exclude core EW0408-26/66JC from the compilation  
796 (Praetorius and Mix, 2014); this core is located in close proximity to the terminus of  
797 a glacier and comparing the  $\delta^{18}O_{\text{calcite}}$  data of this core to other cores within the subpolar  
798 gyre demonstrates planktic foraminiferal  $\delta^{18}O_{\text{calcite}}$  data from this core primarily reflect  
799 local meltwater changes, rather than wider oceanographic conditions in the subpolar  
800 gyre (Figure S3). The compiled dataset will be available on Pangea.



801

802 **Figure S7** Foraminiferal  $\delta^{18}\text{O}_{\text{calcite}}$  from the subpolar gyre over deglaciation. A GAM fit with to all the  
 803 data (excluding core EW0408-26/66JC) is shown by the purple line, with standard error of the fit shaded.  
 804 Data from core EW0408-26/66JC (Praetorius and Mix, 2014) is shown in green.

805

### 806 *Seasonality of planktic foraminifera*

807 Our approach assumes that any change in seasonal bias relating to the habitat preference  
 808 of foraminifera are small relative to the change in temperature due to the movement of  
 809 the gyre boundary. The validity of this approach is supported by sites where  $\delta^{18}\text{O}_{\text{calcite}}$   
 810 has been measured on more than one species of foraminifera, such as core ODP Site  
 811 893 (Figure 1 and Figure 2). At this site, foraminiferal species with habitat temperature  
 812 preferences that are known to be different (*G. bulloides* and *N. pachyderma*, e.g. Taylor  
 813 *et al.*, 2018) show very similar changes down core, with a Holocene-LGM change that  
 814 is identical (within error); this suggests any changes relating to changes seasonal bias  
 815 are likely to be insignificant in our reconstruction.

816

817

818 *Sea surface temperature compilation*

819 We compiled Mg/Ca and  $U^{K'}_{37}$  sea surface temperature (SST) data from across the  
820 North Pacific (Mg/Ca: Reitdorf et al., 2013; Gebhardt et al., 2008; Rodriguez Sanz et  
821 al., 2013; Taylor et al., 2015; Sagawa et al., 2006; Sagawa et al., 2008; Pak et al., 2012;  
822 Kubota et al., 2010; Gray et al., 2018.  $U^{K'}_{37}$ : Minoshima et al., 2007; Seki, 2004; Harada  
823 et al., 2004; Harada, 2006; Harada et al., 2008; Inagaki et al., 2009; Herbert et al., 2001;  
824 Sawada et al., 1998; Yamamoto et al., 2004; Isono et al., 2009). All age models are as  
825 given in the original publication. All Mg/Ca and  $U^{K'}_{37}$  data were recalibrated (see  
826 below) and the temperature change during the LGM is given as a difference to both  
827 proxy temperature in the Holocene, and to mean annual climatological temperature  
828 from the WOA13 (Boyer et al., 2013).

829 While the direct temperature sensitivity of Mg/Ca in planktic foraminifera is ~6% per  
830 °C (Gray et al., 2018b; Gray and Evans, 2019), due to the effect of temperature on pH  
831 through the disassociation constant of water ( $K_w$ ), the ‘apparent’ Mg/Ca temperature  
832 sensitivity is higher (Gray et al., 2018b). Thus, we calculate the change in temperature  
833 from the change in Mg/Ca at each site using a temperature sensitivity of 8.8%, derived  
834 from laboratory cultures (Kisakürek et al., 2008), which encompasses both the direct  
835 temperature effect and the temperature-pH effect, with a Mg/Ca-pH sensitivity of ~ -  
836 8% per 0.1 pH unit (Lea et al., 1999; Russell et al., 2004; Evans et al., 2016; Gray et  
837 al., 2018b; Gray and Evans, 2019). Mg/Ca is also influenced by salinity, with a  
838 sensitivity of ~4% per PSU (Hönisch et al., 2013; Gray et al., 2018b; Gray and Evans,  
839 2019). We make no attempt to account for the effects of salinity (due to sea level) or  
840 pH downcore (due to lower atmospheric CO<sub>2</sub>). The combined effect of the whole-ocean  
841 increase in salinity (due to sea level), and the increase in surface ocean pH (due to lower  
842 atmospheric CO<sub>2</sub>) means changes in temperature derived from changes in Mg/Ca are

843 likely to be cold-biased by  $\sim 1.5$  °C during the LGM (Gray and Evans, 2019). For UK<sup>K</sup><sub>37</sub>,  
844 the change in temperature at each site was calculated using the calibration of Prah1 et  
845 al., 1988; the temperature range in this study is too low to be substantially effected by  
846 the non-linearity of UK<sup>K</sup><sub>37</sub> (e.g. Tierney and Tingley, 2018).

847

#### 848 *General Circulation Models*

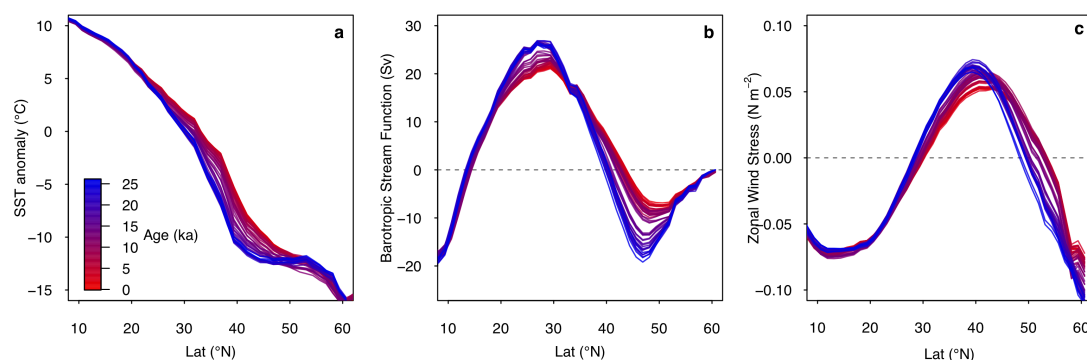
849 We assess differences in North Pacific barotropic stream function, wind stress curl,  
850 zonal wind stress, and SST between LGM and pre-industrial conditions as represented  
851 by five coupled climate models (CCSM4, CNRM-CM5, MPI-ESM-P and MRI-  
852 CGCM3). All models are part of the Coupled Model Intercomparison Project phase 5  
853 (CMIP5, Taylor et al., 2012). We only used models where both wind stress and  
854 barotropic stream function data are available. Orbital parameters, atmospheric  
855 greenhouse gas concentrations, coastlines and ice topography for the LGM simulations  
856 are standardized as part of the Paleoclimate Model Intercomparison Project phase 3  
857 (PMIP3) (Braconnot *et al.* 2012, Taylor *et al.* 2012). Ensemble means are computed by  
858 first linearly interpolating to a common grid.

859

860 Using a single model (HadCM3) we look at runs where the model greenhouse gas, ice  
861 sheet albedo, ice sheet topography are changed individually ('Green Mountains, White  
862 Plains') as described in Roberts and Valdes (2017). The 'Green Mountains, White  
863 Plains' runs use the ICE5G ice sheet reconstruction (Peltier *et al.*, 2004), whereas the  
864 deglacial 'snapshot' runs (below) use the ICE6G ice sheet reconstruction (Peltier *et al.*,  
865 2015).

866

867 We also explore changes through time over the deglaciation using a series of HadCM3  
868 equilibrium-type simulations where all forcings and model boundary conditions are  
869 changed at 500-year intervals broadly adhering to the PMIP4 last deglaciation protocol  
870 (Ivanovic et al., 2016). These simulations use the ICE6GC ice sheet reconstruction and  
871 'melt-uniform' scenario for ice sheet meltwater; i.e. freshwater from the melting ice  
872 sheets is NOT routed to the ocean via coastal outlets. Instead, water is conserved by  
873 forcing the global mean ocean salinity to be consistent with the change in global ice  
874 sheet volume with respect to present. Note, these deglacial simulations are not transient,  
875 but are equilibrium-type experiments that begin from the end of the 1750-year long  
876 simulations run by Singarayer et al. (2011). At each 500-year interval (21.0 ka, 20.5 ka,  
877 20.0 ka...0.5 ka, 0.0 ka), all boundary conditions and forcings are updated according to  
878 the more recent literature (presented by Ivanovic et al., 2016) and held constant for the  
879 full 500-year duration of the run. The climate means and standard deviations used here  
880 are calculated from the last 50 years of each simulation (i.e. year 451-500, inclusive).  
881 More information on these runs can be found in the supplement to Morris et al. (2018),  
882 noting that we use the raw model output and not the downscaled and bias-corrected  
883 data used in the previous publication.



884

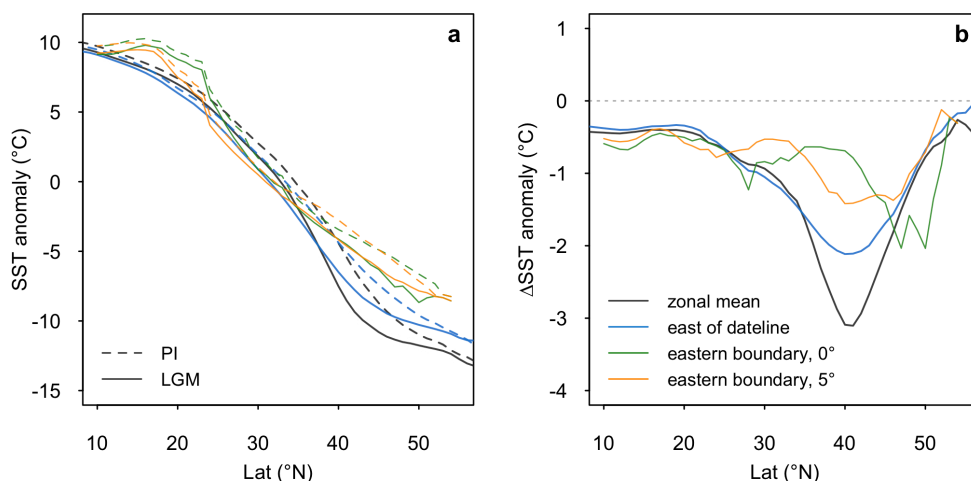
885 **Figure S8** Deglacial evolution of zonal mean (a) SST anomaly (relative to global mean) (b) barotropic  
886 stream function (c) zonal wind stress in the HadCM3 simulations.

887

888

889 *Eastern boundary test*

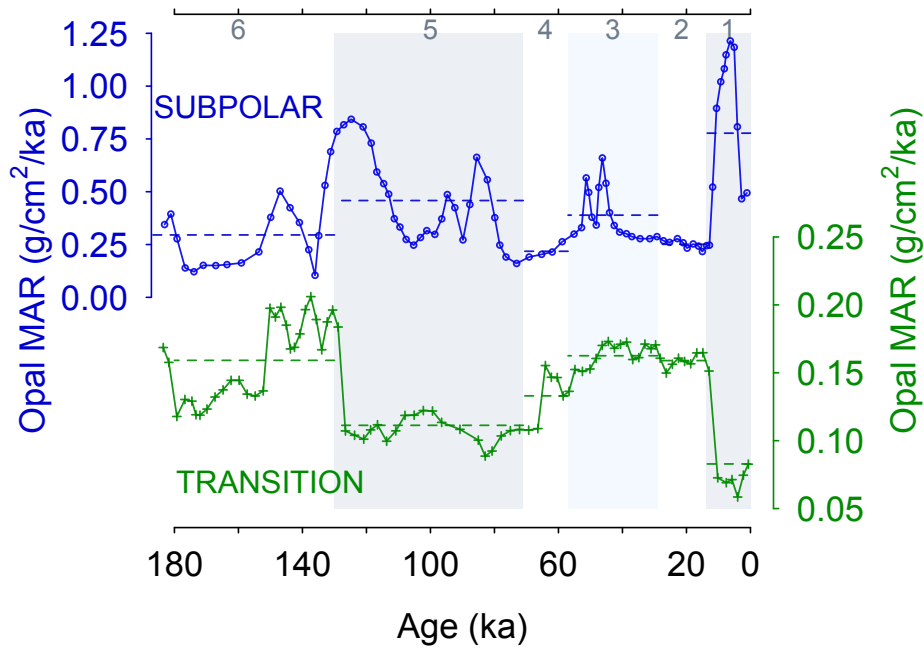
890 To test if there is an influence of coastal upwelling on the data in the east (i.e. a signal  
891 of some other control on latitudinal temperature anomaly [and thus latitudinal  $\delta^{18}\text{O}_{\text{calcite}}$   
892 anomaly] besides change in gyre position) we compare the ensemble mean SST along  
893 the eastern boundary of the basin (taken as the first oceanic grid point west of land  
894 during the LGM) to the zonal mean, and zonal mean east of the dateline (Fig. S9). The  
895 models show no indication of a strong influence of coastal upwelling, which would  
896 manifest as an anomalous cooling relative to the zonal mean. This analysis suggests  
897 coastal upwelling is unlikely to be having a significant effect on our results, although  
898 the simulated coastal upwelling may be poorly represented due to the resolution of the  
899 models. A further argument against a strong influence of upwelling on the data in the  
900 East Pacific is that sites that are  $\sim 15^\circ$  apart from each other latitudinally, such that they  
901 are in different upwelling regimes today and are likely to have undergone very different  
902 changes in upwelling since the LGM, display very similar patterns of change in  
903  $\delta^{18}\text{O}_{\text{calcite}}$  over deglaciation, with no differences in timing (Fig. 1).



904

905 **Figure S9 (a)** LGM and PI SST anomaly (from global mean), and **(b)** LGM-PI SST anomaly in different  
906 longitudinal bins; zonal mean (grey), zonal mean east of the dateline (180°, blue), along the eastern  
907 boundary of the basin (green), and 5° seaward from the eastern boundary of the basin (orange). Note, the  
908 gyre boundary is located slightly further north along the eastern margin relative to the zonal mean and  
909 zonal mean east of the dateline.

910



911

912 **Figure S10** Opal Mass Accumulation Rate data from core KH99-03 in the SPG (Narita et al., 2002) and  
 913 core NCG108 in the transition zone (Maeda et al., 2002). Dashed lines show mean value for each marine  
 914 isotope stage (MIS). Grey shading shows MIS 1, 3 and 5. Transition zone and subpolar waters show an  
 915 anti-phased relationship in Opal MAR over the last glacial cycle.  
 916

917 *HSI Freshwater test*

918 The release of large amounts of freshwater into the eastern subpolar North Pacific has  
 919 been suggested over deglaciation, at ~17.5 ka (Maier *et al* 2018). The release of  
 920 freshwater into the eastern subpolar North Pacific is evident in an increase in the  
 921  $\delta^{18}\text{O}_{\text{calcite}}$  difference between the mixed-layer dwelling species *G. bulloides* and the  
 922 slightly deeper-dwelling species *N. pachyderma* in core MD02-2489 (54.39°N, -  
 923 148.92°E) at this time; during this interval *G. bulloides* becomes ~0.6‰ more depleted  
 924 than *N. pachyderma*. To test if this release of freshwater may be influencing our gyre  
 925 boundary reconstruction we re-run the gyre-boundary analysis, however removing the  
 926 *G. bulloides* data from core MD02-2489; the results are identical to the gyre boundary  
 927 reconstruction including the *G. bulloides* data demonstrating that the effect of  
 928 freshwater release has very little effect on our gyre boundary reconstruction. This is  
 929 because the change in  $\delta^{18}\text{O}_{\text{calcite}}$  from the freshwater release (~0.6‰, equivalent to ~2

930 PSU freshening) is very small compared to the large change in  $\delta^{18}\text{O}_{\text{calcite}}$  resulting from  
931 the temperature difference between the gyres (6 ‰). Localised freshwater inputs, while  
932 having a large effect locally, do very little to change the pattern of  $\delta^{18}\text{O}_{\text{calcite}}$  at the basin  
933 scale.

934

935

936

937

938

939

940

941

942

943

944

945

946

947

948

949

950

951

952

953

954

955

956

957

958



**Table S1** Compiled planktic foraminiferal  $\delta^{18}\text{O}_{\text{calcite}}$  records. The compiled will be made available on Pangea.

Core	Lat (°N)	Lon (°E)	Species	Reference
MD02-2489	54.39	-148.921	N. pachyderma	Gebhardt et al 2008
MD02-2489	54.39	-148.921	G. bulloides	Gebhardt et al 2008
PAR87A-10	54.363	-148.4667	G. bulloides	Zahn et al 1991
PAR87A-10	54.363	-148.4667	N. pachyderma	Zahn et al 1991
PAR87A-02	54.29	-149.605	G. bulloides	Zahn et al 1991
PAR87A-02	54.29	-149.605	N. pachyderma	Zahn et al 1991
MD02-2496	48.967	-127.033	N. pachyderma	Taylor et al 2015
MD02-2496	48.967	-127.033	G. bulloides	Taylor et al 2015
ODP1017	34.32	-121.6	G. bulloides	Pak et al 2012
ODP893	34.2875	-120.03667	N. pachyderma	Hendy et al 2002
ODP893	34.2875	-120.03667	G. bulloides	Hendy et al 2002
MD02-2503	34.28	-120.04	G. bulloides	Hill et al 2006
AHF-28181	33.011667	-119.06	G. bulloides	Mortyn et al 1996
MD05-2505	25	-112	G. ruber	Rodríguez-Sanz et al 2013
SO201-2-101	58.883	170.683	N. pachyderma	Reitdorf et al 2013
SO201-2-85	57.505	170.413167	N. pachyderma	Reitdorf et al 2013
SO201-2-77	56.33	170.69883	N. pachyderma	Reitdorf et al 2013
SO201-2-12	53.992667	162.375833	N. pachyderma	Reitdorf et al 2013
MD01-2416	51.268	167.725	N. pachyderma	Gebhardt et al 2008
MD01-2416	51.268	167.725	G. bulloides	Gebhardt et al 2008
VINO-GGC37	50.28	167.7	N. pachyderma	Keigwin 1998
LV29-114-3	49.375667	152.877933	N. pachyderma	Reitdorf et al 2013
KT90-9_21	42.45	144.3167	G. bulloides	Oba and Murayama 2004
GH02-1030	42	144	G. bulloides	Sagawa and Ikehara 2008
CH84-14	41.44	142.33	G. bulloides	Labeyrie 1996
CH84-04	36.46	142.13	G. bulloides	Labeyrie 1996
MD01-2420	36.067	141.817	G. bulloides	Sagawa et al 2006
MD01-2421	36.01667	141.7833	G. bulloides	Oba and Murayama 2004
KY07_04_01	31.6391667	128.944	G. ruber	Kubota et al 2010
A7	27.82	126.98	G. ruber	Sun et al 2005
ODP184-1145	19.58	117.63	G. ruber	Oppo and Sun 2005

959

960

961

962

963

964

965

**Table S2** Reconstructed change in gyre boundary latitude. Uncertainty is  $1\sigma$ .

age	DLat	DLat_error	DLat_west	DLat_west_error	Dlat_east	DLat_east_error
10.5	0.0	1.0	0.0	1.3	0	1.0
11.0	-0.6	0.9	-0.7	1.2	-0.3	0.9
11.5	-1.0	0.9	-1.1	1.1	-0.5	1.0
12.0	-1.4	0.9	-1.7	1.1	-0.5	1.1
12.5	-1.5	0.9	-1.9	1.0	-0.8	1.1
13.0	-1.6	0.9	-1.8	1.0	-0.2	1.3
13.5	-1.6	0.9	-1.8	1.0	0	1.3
14.0	-1.5	0.9	-1.7	1.0	0.2	1.3
14.5	-1.5	0.9	-1.7	1.0	-0.5	1.2
15.0	-1.9	0.8	-1.9	1.0	-2.4	1.0
15.5	-2.3	0.8	-2.1	1.0	-3.9	1.0
16.0	-2.6	0.8	-2.1	1.0	-5	0.9
16.5	-2.8	0.9	-2.0	1.0	-5.9	0.9
17.0	-3.1	0.9	-2.0	1.0	-6.3	0.9
17.5	-3.2	0.9	-2.0	1.0	-6.3	1.0
18.0	-3.1	0.9	-2.0	1.0	-6.4	1.1
18.5	-3.1	0.9	NA	NA	-6	1.1

966

967 **Additional References**

- 968 Boyer, T.P., Antonov, J.I., Baranova, O.K., Coleman, C., Garcia, H.E., Grodsky, A., John-  
969 R.A., Mishonov, A.V., O'Brien, T.D., Paver, C.R., Reagan, J.R., Seidov, D., Smolyar, I.V., Zweng, M.M., 2013.  
970 World Ocean Database 2013. In: Levitus, Sydney (Ed.), Alexey Mishonov (Technical Ed.), NOAA Atlas  
971 NESDIS, vol. 72. 209 pp.
- 972 Evans D., Wade B. S., Henehan M., Erez J. and Müller W. (2016) Revisiting carbonate chemistry controls on  
973 planktic foraminifera Mg / Ca: Implications for sea surface temperature and hydrology shifts over the Paleocene-  
974 Eocene Thermal Maximum and Eocene-Oligocene transition. *Clim. Past* 12.
- 975 Gebhardt, H. et al., Paleonutrient and productivity records from the subarctic North Pacific for Pleistocene glacial  
976 terminations I to V. *Paleoceanography* 23, PA4212 (2008).
- 977 Gray, W. R., Weldeab, S., Lea, D. W., Rosenthal, Y., Gruber, N., Donner, B. and Fischer, G. (2018b) The effects of  
978 temperature, salinity, and the carbonate system on Mg/Ca in *Globigerinoides ruber* (white): A global sediment  
979 trap calibration. *Earth Planet. Sci. Lett.* 482, 607–620.
- 980 Gray, W.R. and Evans, D. (2019) Nonthermal influences on Mg/Ca in planktonic foraminifera: A review of culture  
981 studies and application to the last glacial maximum. *Paleoceanography and Paleoclimatology*, 34. [https://doi.org/](https://doi.org/10.1029/2018PA003517)  
982 [10.1029/2018PA003517](https://doi.org/10.1029/2018PA003517)
- 983 Harada, N. Ahagon, N., Uchida, M. (2004) Northward and southward migrations of frontal zones during the past 40  
984 kyr in the Kuroshio-Oyashio transition area. *Geochemistry*, doi:10.1029/2004GC000740/pdf.
- 985 Harada, N. (2006) Rapid fluctuation of alkenone temperature in the southwestern Okhotsk Sea during the past 120  
986 ky. *Global and Planetary Change*. 53, 29–46.
- 987 Harada, N., Sato, M., Sakamoto, T. (2008) Freshwater impacts recorded in tetraunsaturated alkenones and alkenone  
988 sea surface temperatures from the Okhotsk Sea across millennial-scale cycles. *Paleoceanography*. 23, PA3201.
- 989 Harada, N., Sato, M., Sakamoto, T. (2008) Freshwater impacts recorded in tetraunsaturated alkenones and alkenone  
990 sea surface temperatures from the Okhotsk Sea across millennial-scale cycles. *Paleoceanography*. 23, PA3201.
- 991 Hendy, I. L., Kennett, J. P., Roark, E. B., Ingram, B. L., (2002) Apparent synchronicity of submillennial scale climate  
992 events between Greenland and Santa Barbara Basin, California from 30-10 ka. *Quaternary Science Reviews* 21,  
993 1167-1184.
- 994 Herbert, D. et al. (2001) Collapse of the California Current During Glacial Maxima Linked to Climate Change on  
995 Land. *Science*. 293, 71–76.

996 Hill, T.M., J.P. Kennett, D.K. Pak, R.J. Behl, C. Robert, and L. Beaufort. 2006. Pre-Bolling warming in Santa  
997 Barbara Basin, California: surface and intermediate water records of early deglacial warmth. *Quaternary Science*  
998 *Reviews* 25, pp. 2835–2845, doi:10.1016/j.quascirev.2006.03.012

999 Hönisch B., Allen K. a., Lea D. W., Spero H. J., Eggins S. M., Arbuszewski J., deMenocal P., Rosenthal Y., Russell  
1000 A. D. and Elderfield H. (2013) The influence of salinity on Mg/Ca in planktic foraminifers – Evidence from  
1001 cultures, core-top sediments and complementary  $\delta^{18}\text{O}$ . *Geochim. Cosmochim. Acta* 121, 196–213.

1002 Inagaki, M., Yamamoto, M., Igarashi, Y., Ikehara, K. (2009) Biomarker records from core GH02-1030 off Tokachi  
1003 in the northwestern Pacific over the last 23,000 years: Environmental changes during the last deglaciation.  
1004 *Journal of Oceanography*. 65, 847–858.

1005 Isono, D. et al. (2009) The 1500-year climate oscillation in the midlatitude North Pacific during the Holocene.  
1006 *Geology*. 37, 591–594.

1007 Kisakürek, B., Eisenhauer, A., Böhm, F., Garbe-Schönberg, D., Erez, J., 2008. Controls on shell Mg/Ca and Sr/Ca  
1008 in cultured planktonic foraminiferan, *Globigerinoides ruber* (white). *Earth Planet. Sci. Lett.* 273, 260–269.  
1009 <https://doi.org/10.1016/j.epsl.2008.06.026>.

1010 Kubota, Y., K. Kimoto, R. Tada, H. Oda, Y. Yokoyama, and H. Matsuzaki (2010), Variations of East Asian summer  
1011 monsoon since the last deglaciation based on Mg/Ca and oxygen isotope of planktic foraminifera in the northern  
1012 East China Sea, *Paleoceanography*, 25, PA4205, doi:10.1029/2009PA001891.

1013 Labeurie, L. 1996. Quaternary paleoceanography: unpublished stable isotope records. IGBP PAGES/World Data  
1014 Center for Paleoclimatology Data Contribution Series #1996-036. NOAA/NGDC Paleoclimatology Program,  
1015 Boulder, Colorado, USA.

1016 Lea D. W., Mashiotta T. A. and Spero H. J. (1999) Controls on magnesium and strontium uptake in planktonic  
1017 foraminifera determined by live culturing. *Geochim. Cosmochim. Acta* 63, 2369–2379.

1018 Maeda, L., H. Kawahata and M. Noharta (2002): Fluctuation of biogenic and abiogenic sedimentation on the Shatsky  
1019 Rise in the western north Pacific during the late Quaternary. *Marine Geology* 189, 197-214.

1020 Minoshima, K., H. Kawahata, K. Ikehara (2007) Changes in biological production in the mixed water region (MWR)  
1021 of the northwestern North Pacific during the last 27 kyr. *Palaeogeography, Palaeoclimatology, Palaeoecology*.  
1022 254, 430–447.

1023 Mortyn, P. G., Thunell, R. C., Anderson, D. M., Stott, L. D., Le, J. (1996) Sea surface temperature changes in the  
1024 Southern California Borderlands during the last glacial-interglacial cycle. *Paleoceanography* 11, 415-430.

1025 Narita, H., M. Sato, S. Tsunogai, M. Maruyama, M. Ikehara, T. Nkatsuka, M. Wakatsuchi, N. Harada and U. Ujiie  
1026 (2002): Biogenic opal indicating less productive northwestern North Pacific during glacial stages. *Geophys. Res.*  
1027 *Lett.*, 29(15), 22-1 to 22-4.

1028 Oba, T., Murayama, M. (2004) Sea-surface temperature and salinity changes in the northwest Pacific since the Last  
1029 Glacial Maximum. *Journal of Quaternary Science* 19, 335-346.

1030 Oppo, D. W., and Y. Sun (2005) Amplitude and timing of sea surface temperature change in the northern South  
1031 China Sea: Dynamic link to the East Asian monsoon. *Geology* 33, 785–788.

1032 Pak, D. K., D. W. Lea, and J. P. Kennett (2012) Millennial scale changes in sea surface temperature and ocean  
1033 circulation in the northeast Pacific, 10–60 kyr BP, *Paleoceanography* 27, PA1212, doi:10.1029/2011PA002238.

1034 Peltier, W. R. (2004). Global glacial isostasy and the surface of the Ice-Age Earth: The ICE-5G (VM2) model and  
1035 GRACE. *Annual Review of Earth and Planetary Sciences*, 32(1), 111–149.  
1036 <https://doi.org/10.1146/annurev.earth.32.082503.144359>

1037 Praetorius, S. K., Mix, A. C. (2014) Synchronization of North Pacific and Greenland climates preceded abrupt  
1038 deglacial warming. *Science* 345, 444. DOI: 10.1126/science.1252000.

1039 Prahl, F. G., L. A. Muehlhausen, and D. L. Zahnle (1988), Further evaluation of long-chain alkenones as indicators  
1040 of paleoceanographic conditions, *Geochim. Cosmochim. Acta* 52, 2303–2310.

1041 Reimer, P. J. et al. (2013) IntCal13 and Marine13 radiocarbon age calibration curves 0-50,000 years cal BP.  
1042 *Radiocarbon* 55, 1869–1887.

1043 Reiss, P. T., Ogden, R. T. (2009) Smoothing parameter selection for a class of semiparametric linear models. *Journal*  
1044 *of the Royal Statistical Society B* 71, 505-523.

1045 Riethdorf, J.-R., Max, L., Nürnberg, D., Lembke-Jene, L., Tiedemann, R. (2013) Deglacial development of (sub)  
1046 sea surface temperature and salinity in the subarctic northwest Pacific: Implications for upper-ocean  
1047 stratification. *Paleoceanography*. 28, 91–104.

1048 Rodríguez Sanz, L., Mortyn, P. G., Herguera, J. C., Zahn, R. (2013) Hydrographic changes in the tropical and  
1049 extratropical Pacific during the last deglaciation. *Paleoceanography*. 28, 529–538.

1050 Russell A. D., Hönisch B., Spero H. J. and Lea D. W. (2004) Effects of seawater carbonate ion concentration and  
1051 temperature on shell U, Mg, and Sr in cultured planktonic foraminifera. *Geochim. Cosmochim. Acta* 68, 4347–  
1052 4361.

- 1053 Sagawa, T., Toyoda, K., Oba, T. (2006) Sea surface temperature record off central Japan since the Last Glacial  
1054 Maximum using planktonic foraminiferal Mg/Ca thermometry.
- 1055 Sagawa, T., Ikehara, K. (2008) Intermediate water ventilation change in the subarctic northwest Pacific during the  
1056 last deglaciation. *Geophysical Research Letters* 35, L24702, doi:10.1029/2008GL035133.
- 1057 Seki, O., et al. (2004) Reconstruction of paleoproductivity in the Sea of Okhotsk over the last 30 kyr.  
1058 *Paleoceanography*. 19, PA1016.
- 1059 Singarayer, J.S., Valdes, P.J., Friedlingstein, P., Nelson, S., Beerling, D.J., 2011. Late Holocene methane rise caused  
1060 by orbitally controlled increase in tropical sources. *Nature* 470, 8285. <https://doi.org/10.1038/nature09739>
- 1061 Taylor, B.J., Rae, J.W.B., Gray, W.R., Darling, K.F., Burke, A., Gersonde, R., Abelman, A., Maier, E., Esper, O.,  
1062 Ziveri, P. (2018) Distribution and ecology of planktic foraminifera in the North Pacific: Implications for paleo-  
1063 reconstructions. *Quaternary Science Reviews* 191, 256-274.
- 1064 Taylor, M. A., Hendy, I. L., Pak, D. K. (2014) Deglacial ocean warming and marine margin retreat of the Cordilleran  
1065 Ice Sheet in the North Pacific Ocean. *Earth and Planetary Science Letters*. 403, 89–98 (2014).
- 1066 Tierney J. E. and Tingley M. P. (2018) BAYSPLINE: A New Calibration for the Alkenone Paleothermometer.  
1067 *Paleoceanogr. Paleoclimatology* 33, 281–301.
- 1068 Yamamoto, M., Oba, T., Shimamune, J., Ueshima, T. (2004) Orbital-scale anti-phase variation of sea surface  
1069 temperature in mid-latitude North Pacific margins during the last 145,000 years. *Geophysical Research Letters*.  
1070 31, L16311.
- 1071 Zahn, R., Pedersen, T. F., Bornhold, B. D., Mix, A. C. (1991) Watermass conversion in the glacial subarctic Pacific  
1072 (54°N, 148°W): physical constraints and the benthic-planktonic stable isotope record. *Paleoceanography* 6, 543-  
1073 560.
- 1074